December 2023

N-body simulations of exoplanets and their moons

Lydia Schollmeier

Department of Physics, Lund University

Master thesis supervised by Jens Hoeijmakers

LUND
UNIVERSITY

Abstract

The planet-planet interactions in a many-planet system cannot be analytically calculated. Instead, they have to be investigated by using an N-body simulation. I discuss three questions about the N-body interactions in planetary systems: The first two are on the system 55 Cnc, a system with five known planets around a K-type star. I will first simulate the influence, that the other planets have on the transit timing variations of planet e. The second goal is to understand the behaviour of dust in the environment of 55 Cnc e and to estimate if it can be responsible for the variations in the secondary eclipses which have been observed using visible and infrared photometry with CHEOPS and Spitzer. The third goal is to ascertain if the presence of a moon around a planet of the pulsar PSR B1257+12 could be detectable in the pulse arrival timing of its pulses.

I have done simulations on the variation in transit timings of 55 Cnc e to find the influence of the inclination of the orbits of the other planets in the system. The result is that the orbits would have to be at nearly a right angle to have a measurable effect on planet e's TTVs. Simulations of dust, which planet e might emit, show that the dust can live for several hundred hours. It distributes itself around the star in such a way that it probably does not cause the observed differences in occultation depth. I also simulated the effect a moon around one of the planets of the pulsar PSR B1257+12 would have on the movement of this pulsar. The effect is a measurable signal with an as-yet unidentified hyperperiod. The signal of a moon is different from the signal other sources could produce, such as a fourth planet or the uncertainty of the known planets' masses. This means that it is feasible that with more sustained observations of PSR B1257+12, exomoons may be detectable in the future.

Populärvetenskaplig beskrivning

There are planets that do not orbit around the sun but around another star, such planets are called exoplanets. They are difficult to detect since most of them are not bright enough to be directly observed. There are several indirect detection methods such as the "transit method", where the planet transits in front of the star and obscures a part of it. This leads to a decrease in the brightness of the star, which can be measured. Another method to detect exoplanets is the "radial velocity method". This method uses the fact that the gravity of the planet pulls the star in its direction. The movement of the star causes a change in the observed light due to the Doppler effect. This means that the wavelength of the light changes in dependence on the star's movement.

Both methods can measure the period of the planet's orbit and thereby the distance between the star and the planet. The radial velocity method can also measure the mass of the planet if the angle between the orbit and the line of sight is known and the transit method can measure the angle of the orbit. The problem is that not all planets can be observed with both techniques. The planet has to pass directly in front of the star in order to be observed with the transit method and this is only for rather few planets the case.

If several planets are orbiting one star, those planets will interact with each other. Those interactions could result in a small disturbance in the orbit, which could be seen in a slightly changed transit timing. The interactions between the planets depend on the angle at which they stand to each other. This means that it could be possible to determine the angle of the orbits of planets that do not transit by observing one planet in the system that does transit. I will do that in the first part of my thesis by simulating the system called 55 Cnc and determining if the effect of the angle between the planetary orbits is large enough to be observed.

The angle between the planetary orbits is not the only unknown thing in this system. There have been measurements of the "secondary eclipse" which is in some sense the opposite of a transit: The planet, which reflects light, moves behind the star and the light, that this planet reflects, is no longer visible. This leads to a decrease in the measured brightness. The measurements of the secondary eclipse were different every time it was observed, which is surprising. There is the possibility of dust that surrounds the planet to reflect light from the star. If this dust cloud changes, it would explain, why we see a different amount of light every time. The second part of my thesis is a simulation of the behaviour and lifetime of dust to find out if it could be responsible for the strange measurements.

Since there are many moons orbiting the planets in the solar system, it is reasonable to assume that some if not many exoplanets have moons as well. So far none have been detected because they are much lighter than the planets and therefore harder to detect. I will simulate in the third part of my thesis the effect on the signal, that a moon would have that orbits in the exoplanet system PSR B1257+12.

Contents

1 Introduction **6**

2 Theory/Background **7**

2.1 Radial velocity method 7

2.2 Transit method 9

2.3 Exomoons 12

2.4 55 Cnc 13

2.5 Dust 15

2.5.1 Ways of emitting dust 15

2.5.2 Behaviour and properties of dust particles 16

2.6 Pulsar Planets 19

3 Method **21**

3.1 N-body simulations 21

3.2 Transit timing variation/WASP-47 22

3.2.1 The model for TTVs 23

3.2.2 Tests on WASP-47 24

3.3 Dust particles 26

3.4 Pulsar planets 30

4 Results/Discussion **33**

4.1 Transit timing variation/55 Cnc 33

4.2 Dust particles 34

4.3 Pulsar timing varitaions 39

5 Conclusion **45**

A Transit timing variations **47**

B Dust particles **49**

List of Figures

2.1 Influence of the inclination on the radial velocity measurement 8
2.2 Overview of all confirmed exoplanets 10
2.3 Transit method 10
3.1 Geometry of the transit detection 23
3.2 Transit timing variation for WASP-47 25
3.3 Transit timing variation for WASP-47 d 26
3.4 Cross-section for different particles sizes, Planck function and β-factor . . . 29
3.5 Pulse timing variation for the planets 31
3.6 Influence of the N-body interaction 32
3.7 Influence of the N-body interaction of planets B and C 32
4.1 Transit timing variation for 55 Cnc e 35
4.2 Mass-loss rate and radius development for a stationary particle 35
4.3 Behaviour of stationary dust particles 36
4.4 Behaviour of dust around planet e 38
4.5 Pulse timing with an Earth-mass moon for planet B 40
4.6 Pulse timing with an Earth-mass moon for planet B 40
4.7 Pulse timing with an Earth-mass moon for planet B 41
4.8 Effect of breaking the resonance between the planets 43
4.9 Fourier transformed pulse timing variation 44
4.10 Pulse timing with a moon for planet C or another planet 45
4.11 Pulse timing with a fourth planet and normal mass for the other planets . 46
4.12 Influence of the uncertainty of the planet mass for planet C 46
4.13 Influence of the uncertainty of the planet mass for planet C 47

List of Tables

3.1 Planetary parameters for WASP-47 24
3.2 Planetary parameters for 55 Cnc 27
3.3 Planetary parameters PSR B1257+12 30

3.4 Parameters for the pulsar moons 33
4.1 Lieftime of dust particles 37

1 Introduction

Exoplanets are planets that do not orbit the sun. They have been studied for almost three decades, the first detection of a planet around a sun-like star by Mayor and Queloz [1995] was rewarded with the Nobel Prize in 2019. Even before that, objects of planetary masses were detected by Wolszczan and Frail [1992] around a pulsar. Since then more than 5,000 exoplanets have been detected with a variety of different methods. Exoplanets are in most cases too close to their host star and in comparison too faint to be directly observed. Most of the exoplanets have therefore been indirectly detected. Planets that are heavy and close to their host stars are easier to detect with those methods, which can be a reason for the large number of detections of such planets.

There are no massive planets close to the sun in the solar system, which makes a difference between the history of such a system and the solar system likely. Such a history could include the migration of planets i.e. a change in their semi-major axis, which can be combined with a change in eccentricity or angle of the orbit with respect to the orbits of the other planets in the system and the spin-axis of the star (Smadar Naoz [2012]). In order to infer something about the history of a system, it is necessary to know the current parameters of the system as well as possible with the limited ways in which we can observe them.

Planets close to their host hosts do not have to be alone in their systems. There are compact systems, which means that many planets have orbits that are close to each other, some of those compact systems are close to their host stars. I will study the dynamic properties of the system 55 Cnc, which is such a compact system, to evaluate if simulations of the interaction between planets can in this system help to limit the possible parameters. The parameters I will simulate in the first part of my thesis are the inclinations of the orbits of the non-transiting planets. I will simulate the effect they have on the transit timing variations of planet e to see if they can be inferred from such a measurement.

The planets themselves and their parameters are not the only interesting objects in exoplanet systems. There my be many smaller objects such as asteroids or even dust. Dust clouds inside a planetary system could influence the measurements by reflecting or blocking light. In the second part of my thesis, I will simulate the behaviour and lifetime of such hypothetical dust particles in the system 55 Cnc.

The third part of my thesis is about exomoons, which are satellites orbiting exoplanets. No exomoons have been detected yet but since almost all planets in the solar system have at least one moon, it is likely that some exoplanets also have moons. Exomoons are difficult to detect because they are much smaller and lighter than exoplanets. I will simulate the signal that would come from a moon around one of the planets in the system PSR B1257+12, in which the planetary masses can be measured very exactly.

My thesis is structured as follows: in Section 2 I explain the background and underlying physical concepts. In Section 3 I explain the methods I used and the way my simulations

work. In Section 4 I discuss my results and in Section 5 I summarise the work and discuss future prospects.

2 Theory/Background

Let us first look at the underlying concepts of this topic. I start this section by explaining how exoplanets can be detected and go on to describe exomoons. I then introduce the 55 Cnc system and discuss the behaviour of dust and end with pulsar planets.

2.1 Radial velocity method

There are two methods to detect exoplanets, which are relevant to my thesis. The first one is called the radial velocity method, which uses the radial velocity of a star. It uses the fact that the star and the planet are orbiting around the centre of mass, which means that the star moves if it has a planet. This implies that the spectrum of the star will have a blue or red shift (changing with the orbiting period of the planet) due to the Doppler effect. This can be measured with a spectrograph. The periodicity makes it possible to be very confident that it comes from a planet if the star is observed for a longer time. Mayor and Queloz [1995] used this method to discover the first exoplanet around a sun-like star for which the were rewarded with the Nobel Prize 2019.

With this method, it is only possible to measure the component of the star's velocity in the direction of sight. The angle between the plane of the sky and the plane of the planet's orbit is called inclination. If the orbit of the planet is in the line of sight, it is defined to have an inclination of 90°. Those orbits are seen "edge-on". Orbits that lie in the plane of the sky have an inclination of 0°, they are seen "face-on". If the orbit of the planet does not have an inclination of 90°, we will get a weaker signal. With only this measurement, there is no way to distinguish a lighter planet with an orbit in the line of sight from a heavier planet with an inclined orbit as shown in Fig. 2.1, which is why one only gets the minimal mass of the planet. This means that it only measures $\sin(i) \cdot m_p$ where i is the inclination and m_p is the mass of the planet.

After discussing the concept qualitatively, let us look at a way to quantify this for the example of a system with only one star and one planet. Setting the origin of the coordinate system at the centre of mass means that the vector pointing to the planet and the vector pointing to the star are always in opposite directions. Since the length of these vectors weighted by the masses must be the same, it follows that

$$M_\star \vec{r}_\star + m_p \vec{r}_p = 0 \tag{2.1}$$

where $M_\star$ and m_p are the masses of the star and the planet and $\vec{r}_\star$ and $\vec{r}_p$ are the position vectors of the star and the planet. This can be rewritten by defining the vector from the

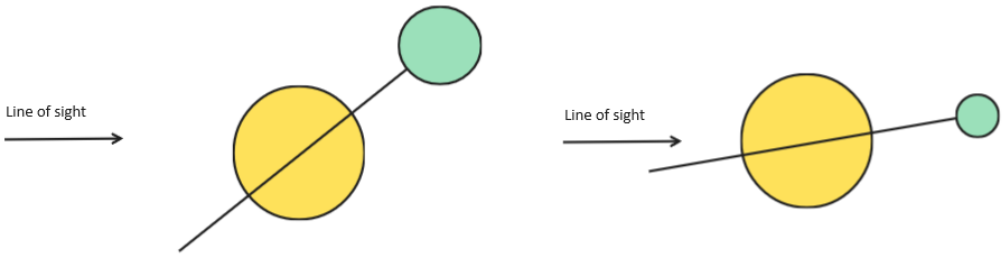

Figure 2.1: The figure shows a star with a heavy planet that has an orbit at an angle with respect to the line of sight and a lighter planet that has an orbit almost aligned with the line of sight. Since the radial velocity method can only detect the part of the star's velocity in the radial direction i.e. in the line of sight, those two planets would create the same signal.

star to the planet $\vec{r} := \vec{r}_p - \vec{r}_\star$ as

$$M_\star \vec{r}_\star + m_p(\vec{r} + \vec{r}_\star) = 0 \tag{2.2}$$

This can be solved for the position vectors:

$$\vec{r}_p = \frac{M_\star}{m_p + M_\star} \cdot \vec{r} \approx \vec{r} \tag{2.3}$$

$$\vec{r}_\star = -\frac{m_p}{m_p + M_\star} \cdot \vec{r} \approx -\frac{m_p}{M_\star} \cdot \vec{r} \tag{2.4}$$

If we now differentiate those two equations, we get the velocities of the star ($\vec{v}_\star$) and the planet ($\vec{v}_p$):

$$\vec{v}_p = \frac{M_\star}{m_p + M_\star} \cdot \vec{v} \approx \vec{v} \tag{2.5}$$

$$\vec{v}_\star = -\frac{m_p}{m_p + M_\star} \cdot \vec{v} \approx -\frac{m_p}{M_\star} \cdot \vec{v}_p \tag{2.6}$$

Assuming a circular orbit and using Newton's law, gives:

$$|\vec{v}_\star| \approx -\frac{m_p}{M_\star} \cdot \sqrt{\frac{GM_\star}{a}} \tag{2.7}$$

where G is the gravitational constant and a the semi-major axis. This is the velocity of the star. But, as discussed above, it is only possible to measure the part of the radial

component of the velocity:

$$K_\star = \sin(i) \cdot |\vec{v}_\star| \approx -\frac{\sin(i) \cdot m_p}{M_\star} \cdot \sqrt{\frac{GM_\star}{a}} \tag{2.8}$$

The semi-major axis cannot be directly measurable for a planet detected with this method, but the orbiting period P can. The third Keplerian law relates those two:

$$\frac{a^3}{P^2} = \frac{G \cdot (M_\star + m_p)}{4\pi^2} \approx \frac{GM_\star}{4\pi^2} \tag{2.9}$$

With this Eq. 2.8 becomes:

$$K_\star \approx \sqrt[3]{\frac{2\pi G}{P}} \cdot \frac{\sin(i) \cdot m_p}{\sqrt[3]{M_\star^2}} \tag{2.10}$$

The velocity of the sun due to the Earth is 0.09 m/s and due to Jupiter it is 12.5 m/s. It would be very difficult to observe the Earth in this way, but Jupiter could be found. Fig. 2.2 shows all detected exoplanets and it is visible from this plot that Jupiter is at a distance, which is the upper limit for the detection with the radial velocity method. But such planets have been discovered, while the Earth is too small to be detected by the radial velocity method.

This method is a useful tool in determining if a star has a planetary companion. Mayor and Queloz [1995] discovered the first exoplanet around a main-sequence star using this method for which they were rewarded with the Nobel Prize in Physics 2019. But even before that Wolszczan and Frail [1992] found a planet around a pulsar with a very similar method that also uses the radial velocity. One of the planetary systems, which have been observed with the radial velocity method, is the WASP-47 system Vanderburg et al. [2017], which I will use later.

2.2 Transit method

The transit method is another way to observe exoplanets, where the planet transits in front of the star and obscures a part of it as shown in Fig. 2.3a. This leads to a decrease in brightness that can be measured. The first planet that was discovered in this way was HD 209458 b by Charbonneau et al. [2000].

This method can, unlike the radial velocity method, only be used for planets in a very narrow range of inclinations. The planet must pass directly between the star and the observer as shown in Fig. 2.3b. Let us now look at the probability of that. The larger the distance between star and planet (a) the smaller the maximal angle at which a transit is observable (Θ). The angles of planetary orbits are randomly distributed between different systems. If we have a certain semi-major axis a, the whole sphere with possible orbits has a surface of $A = 4\pi a^2$. The part of the sphere on which a planetary orbit could be seen

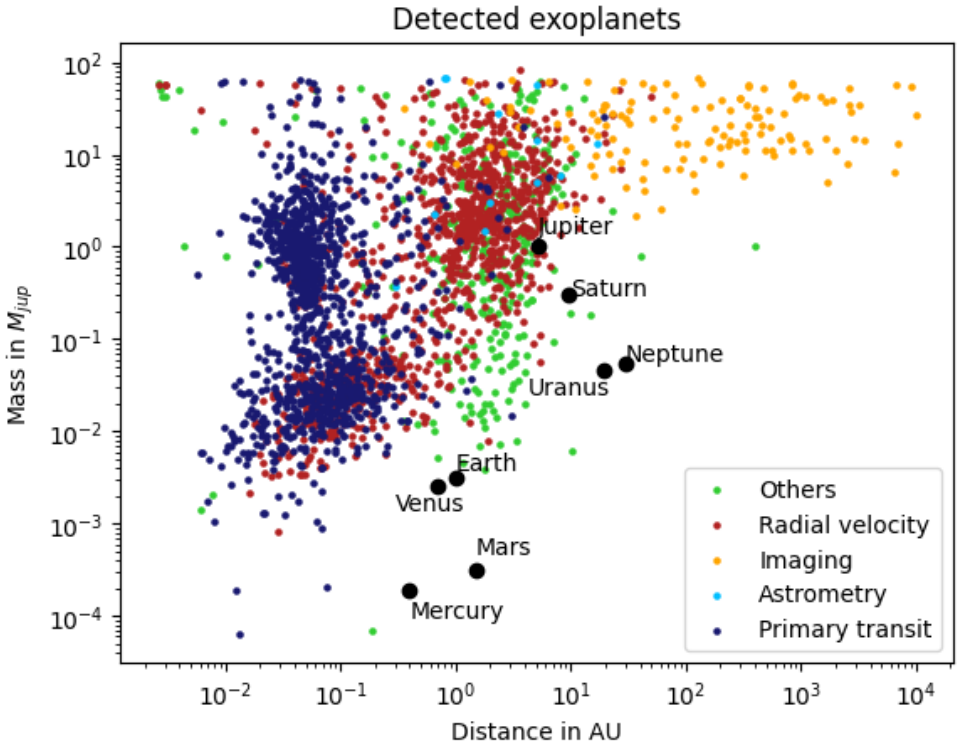

Figure 2.2: All confirmed exoplanets and their method of detection as a function of their semi-major axis and mass. (The data is taken from `https://exoplanet.eu/catalog/`.)

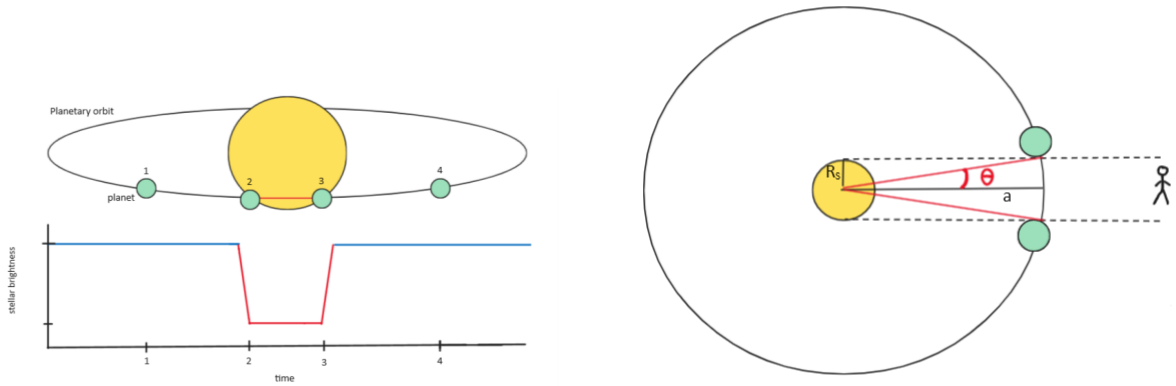

(a) Transiting planet

(b) Transit probability and duration

Figure 2.3: The orbit of a transiting planet and the apparent decrease of the star's luminosity (left). A schematic representation of the points in the orbit along which an exoplanet blocks light from its host star in the transit event (right).

to transit is a stripe of the thickness $2R_\star$ around the sphere. This means the part of the sphere, where the planet could be is $A' = 4\pi a R_\star$. The probability for any planet to transit is

$$p = \frac{A'}{A} = \frac{4\pi a R_\star}{4\pi a^2} = \frac{R_\star}{a} \tag{2.11}$$

which leaves the range of inclinations at which a planet can transit to be $2\Theta = \frac{R_\star}{a}$. The transit probability for Earth is 0.5% and for Jupiter, it is 0.09%.

The next question is if such a transit would be detectable. This is determined by the so-called transit depth, the decrease in brightness or flux of the star. Assuming that the star is a homogeneous disc, means that the flux is proportional to the surface of the star and the decrease in flux depends only on the part of the star that is obscured by the planet. The star has a surface of $A_\star = \pi R_\star^2$ and the planet has a surface of $A_p = \pi R_p^2$. The relative decrease in flux is thereby given by

$$\frac{F - F'}{F} = \frac{\Delta F}{F} = \frac{R_p^2}{R_\star^2} \tag{2.12}$$

which is 0.008% for Earth and 1.06% for Jupiter. This is only an approximation because a real star is not completely homogeneous. A star can have star spots and a star is always less bright at the edges (limb darkening).

A transit lasts only for a short time, compared to the orbiting period P. This transit duration can be calculated (for a circular orbit) by multiplying the orbiting period with the fraction of the angles during which the transit is observable. In Fig. 2.3b it is visible that the transit spans an angle of 2Θ. The duration d is therefore

$$d = P\frac{2\Theta}{2\pi} \approx \frac{P R_\star}{a\pi} \tag{2.13}$$

which would be 0.54 d for Earth and 1.23 d for Jupiter.

Another effect connected with the stellar flux during the transit is the Rossiter-McLaughlin effect. This effect uses the circumstance that the spectrum of the star is Doppler-broadened due to its rotation. The part that moves towards us is blue- and the part that moves away from us is red-shifted. Since the planet only obscures a small part of the star at a time, measuring the Rossiter-McLaughlin effect can detect the spin-orbit alignment if the rotation of the star is known. This has for example been done by Kyle Hixenbaugh [2023], Josette Wright and Wang [2023] and Jiayin Dong [2023].

So far we have only looked at a single planet orbiting a star, but the interactions between several planets in the same system can also be measured by observing the transits. The timing of transit events varies with the perturbation of the Keplarian orbit due to the gravitational influence of other planets in the same system. These transit timing variations (short TTVs) can be (taking Grimm, Simon L. et al. [2018] as an example) detected

accurately in the order of minutes. The perturbations depend on the angles between the orbits, the distances between the orbits and the masses of the planets. Holman and Murray [2005] first proposed that these timing variations could be used to detect other planets in the system by their gravitational interaction with the transiting one. This could be observed by a small change in the timing of the transit compared with the expected timing for a Keplarian orbit or by the influence of only the other known planets. I will examine the interaction between the planets of 55 Cnc by simulating the TTVs of planet e after I tested my simulation on the system of WASP-47, which has three transiting planets of which the TTVs are known.

After having discussed the properties of a planet's transit in front of a star, let us look at a planet which moves behind its host star. The planet reflects light from the star, but we can only see this light if we are looking at the dayside of the planet. So right before and after transit, we see only the night side of the planet. But right before the planet moves behind the star (the so-called occultation or secondary eclipse) we see almost the full dayside. This means that we see the star's luminosity plus the light reflected (and emitted) by the planet right before and after the occultation and during the occultation we can only see the luminosity of the star. The depth of the occultation depends on the size, albedo, temperature of the planet and the wavelength. All of those are properties that do not change the flux inside the secondary eclipse, which is constant. Unlike the transit, where the planet can move in front of starspots, the secondary eclipse has always a constant depth throughout its whole duration. The depth of the secondary eclipse can vary if the planet has an atmosphere. This atmosphere could change in its reflectivity for example due to clouds, which would lead to a change in the depth of the secondary eclipse.

2.3 Exomoons

Many exoplanets have been found with the methods described above. It is not something extraordinary that a star has a planetary companion, there are 4900 confirmed exoplanets (Li et al. [2023]), and there are also many systems with several planets. Since there are many moons orbiting the planets in the solar system, it is reasonable to assume that some if not many exoplanets have satellites. There have been many attempts to find exomoons as well as studies that try to gain a theoretical understanding of how exomoons might behave in a specific system (for example Sucerquia et al. [2021]). But no exomoons have been observed jet.

Another approach is to create an overview of how the orbits of exomoons would statistically be expected to evolve in compact systems, which Hansen [2022] did. They found, in agreement with Tokadjian and Piro [2020], that the orbits of both large and small exomoons would easily become unstable and that there is only a small ratio between the planet and satellite mass and the distance from the planet, allowing for a stable orbit. The exomoons on orbits that are too close to the planet, will eventually collide with the planet. For moons that are too far away from the planet, the evolution is a bit more complicated: The

moon would spiral outwards, eventually escaping the gravity of the planet. For a planet that is very close the its star, the moon would probably not escape the system due to the strong gravitation of the star. Since the former moon has a similar velocity and angular momentum as its former host planet, it will eventually end up on an orbit that is very similar to the orbit of this planet. All the moons in their simulation that escaped the planet's gravitation at some point collide with their host planet.

Hansen [2022] found that a moon could only be stable if it was closer to its host planet than half the Hill-radius. The Hill radius is the distance from the planet, in which the gravitational force of the planet is stronger than that of the star. It is given by

$$R_H = a\sqrt[3]{\frac{m_p}{3 \cdot (m_p + m_s)}} \tag{2.14}$$

where a is the semi-major axis of the planet's orbit, m_p is the mass of the planet and m_s is the mass of the star. The moon must also be farther away than the Roche radius from the planet. The Roche radius is the distance at which a moon would get tidally disrupted by the planet's gravitation due to a strong gradient in the gravitational field within the moon. It is given by

$$d = R_p\sqrt[3]{\frac{\rho_p}{\rho_m}} \tag{2.15}$$

where R_p is the radius of the planet, ρ_p the density of the planet and ρ_m the density of the moon. The fact, that it depends on the density of the moon, makes it different for different moons, while the Hill radius is the same for all satellites. The Roche radius cannot be exactly known for exomoons. Not only because the moon's density cannot be known before it is detected, but even the density and radius of the planet are not always known. It is however possible to guess the Roche radius in many cases. From the mass of the planet and the distance from its host star, one can derive a guess of whether it is a gas giant, an ice giant or a rocky planet. From this guess of the density, one can derive the radius. The density of the moon is harder to guess but a rocky planet for example is unlikely to have a gaseous moon. The densities are in a third root, which makes the uncertainty on the densities less important than that on the radius.

2.4 55 Cnc

The system I will mainly study in this thesis is the 55 Cnc system. 55 Cnc is a binary star with one red dwarf and one K-type star, which can be seen with the naked eye. There are 5 known planets orbiting the K-type star. The first planet discovered in this system was planet b 1997 by Butler et al. [1997]. This is a gas giant which was later found to be in a 3:1 resonance with planet c, which was discovered in 2002 by Marcy et al. [2002]. The same paper announced the discovery of planet d, a gas giant on a Jupiter-like orbit. Only two years later an ultra-short period (0.736547 ± 10^{-6} days (Zhao et al. [2022]))

super-Earth, planet e, was discovered by McArthur et al. [2004] and it was in 2011 found to be transiting by Winn et al. [2011] and Demory et al. [2011]. In 2008 a gas giant in the habitable zone (planet f) was discovered (Fischer et al. [2008]). All those planets were discovered with the radial velocity method, which I described in more detail in Section 2.1. A consequence of the radial velocity method is that the minimum mass is known, but the inclinations of the orbits are unknown. Aschwanden [2018] suggested that there is the possibility for more planets with stable orbits, which have not yet been detected. They argue that harmonic resonances, which are widely known to make planetary (or moon) orbits stable (including examples from the solar system with the 3:2 resonance between Pluto and Neptune), between the orbiting periods of different planets would make those orbits stable.

There is some debate about the most likely inclinations of the orbits of the non-transiting planets. Except for planet d, all the planets are orbiting at a distance within 1 AU from the star, which makes it in this respect, unlike the solar system. This means that there could be a migration history in the system, which is very different from the one in the solar system. A theory for the history of the system has as only restriction the current parameters of the system. Knowing the inclination of the orbits would restrain the allowed parameters and make it easier to infer something about the initial conditions. Some assume more or less coplanar orbits for all the planets (Nelson et al. [2014] or Bourrier, Vincent and Hébrard, Guillaume [2014]). But others (for example Hansen and Zink [2015]) argue for the possibility of a large angle between the orbit of planet e and the other planets in the system. This angle would change the distance between the planets and thereby their interaction. I will simulate this in the first part of my thesis.

In addition to the planets, 55 Cnc has a dust disk with an inclination of 27°(Trilling and Brown [1998]), which has been observed in the infrared (Trilling and Brown [1998], Jayawardhana et al. [2000]). This dust disk seems to be in some respects similar to the dust disk in the solar system, the Kuiper belt. The radius of both is about 40 AU and they have both strong absorption lines that imply methane ice (Trilling and Brown [1998]). The mass of the dust disk might be something between about the same mass of the Kuiper belt (Jayawardhana et al. [2000] and Marcy et al. [2002]) or ten times its mass (Trilling and Brown [1998]). But even with just the mass of the Kuiper belt, it has more dust than would be expected for a star of that age (Jayawardhana et al. [2000]). The dust disk has an inner radius of at least 13 AU (Trilling and Brown [1998]), which means that the dynamics of the planets, which have been detected so far, can be assumed to be uninfluenced by it.

Of all the objects in this system, planet e is probably the one that is most discussed. There has been a lot of debate about the possibility of an atmosphere, some, like Tsiaras et al. [2016], Hammond and Pierrehumbert [2017] and Ehrenreich et al. [2012], argue in favour of an atmosphere, while others like Hansen and Zink [2015] and Zhang et al. [2021] argue against it. There is also the possibility of a mineral-rich atmosphere due to the outgassing from the host planet, which however has not been detected Keles et al. [2022]. Another unknown property of planet e is the angle between its orbit and the spin axis of the star.

The star rotates slowly, which makes the Rossiter-McLaughlin effect (see Section 2.2) too small (López-Morales et al. [2014]) to measure it.

The most extraordinary property of 55 Cnc e is the variation in the occultation depth. The occultation depth should be (almost) the same every time (see Section 2.2 for a detailed explanation), but 55 Cnc e shows a great variation between the observations at different times in far-ultraviolet, visible and infrared (Sulis et al. [2019], Demory, B.-O. et al. [2023]). Demory, B.-O. et al. [2023] found the occultation depth to vary between 166 ppm (parts per million) and -48 ppm. This means not only that the occultation depth can be anything between 166 ppm and not measurable occultation at all, but that the star's measured brightness sometimes increases during the secondary eclipse. The variability is too big to come from starspots (Demory et al. [2016]). There are different ways to explain this variability. Sulis et al. [2019] proposed that an interaction between the star and the planet could be the reason for it. There is also some debate about the magnetic field of the planet and the star and the possibility of an interaction between them (Folsom et al. [2020]). Demory et al. [2016] proposed liquid lava at the dayside of the planet ($T_{max} = (2697 \pm 268)$ K). This might result in lava flows, which might change the surface in such a way, that the reflection changes, which in turn could change the occultation depth. The above-discussed atmosphere could (if it exists) change the reflectivity for example with clouds (Keles et al. [2022]). Another explanation is dust that is emitted by the planet, if it does not have an atmosphere, for example by volcanism due to tidal heating (Jackson et al. [2008] and Bolmont et al. [2013]). This dust could form a torus around the planet, which reflects light and if it comes from volcanic activities, it would explain that its reflectivity is different every time (Demory et al. [2016]).

2.5 Dust

The dust particles are probably the most discussed explanation for the changes in the occultation depth. This discussion has two dimensions: One is the question of how the dust would be emitted and the other, is what would happen to the dust, once it was emitted.

2.5.1 Ways of emitting dust

The question of how the dust gets emitted is mostly answered by the consequences of tidal heating. Jackson et al. [2008] and Bolmont et al. [2013] suggested that tidal heating due to the short distance between the star and the planet, as well as the compactness of the planetary system with four planets, including gas giants, within 1 AU, could lead to tidal heating. This makes it plausible that 55 Cnc e has strong volcanism at its surface. The temperature of the planet is high enough for lava pods to exist, which could lead to outgassing at the dayside (Gelman et al. [2011], Rappaport et al. [2012] and Demory et al. [2016]). But Brogi et al. [2012] suggests that outgassing particles would not have the

velocity to escape the gravitation of a super-earth. The needed escape velocity of 55 Cnc e is 23.2 km/s, which is more than twice the escape velocity of the Earth (11.2 km/s).

If 55 Cnc e had one or several undetected exomoons, there would be many more possibilities for tidal effects and emission of circumplanetary dust. Something similar can be observed in the solar system: Jupiter is surrounded by a huge cloud of atoms and ions sourced by the moons. The rings of Jupiter are sourced by the moons too. Several exomoons could induce tidal heating in each other (Tokadjian and Piro [2023]) similar to the effect the Jupiter moons have on each other. The planet and moon(s) could have tidal interaction leading to tidal heating or volcanism on both planet and moon. The moon could for example prevent the planet's core from cooling down (Andrault et al. [2016]). A moon could also get unstable and collide with the host planet (see Section 2.3 for details). Those collisions would create a lot of dust and larger debris, which will slowly decay into dust. The dust emitted by volcanic activity on Earth has a uniform size distribution (Beckett et al. [2022], Krishnan et al. [2017]). This is different from the dust of a debris disk, which follows a power-law of $\sim r^{-3.7}$ as a size distribution in consequence of the collisional equilibrium (Löhne, T. et al. [2017]).

2.5.2 Behaviour and properties of dust particles

After looking at the different ways to emit dust, let us now look at the second question about dust: What happens if it were to be emitted at a velocity higher than the escape velocity? This is what I will simulate in the second part of my thesis. The first thing to disclaim is that it would be hard to simulate dust in an atmosphere of which we know nothing. It is not known (as discussed above) if an atmosphere exists, I will assume for the following discussion that it does not. I will also assume that the dust particles are not charged and therefore not discuss the influence of electric and magnetic fields.

The motion of dust in a stellar system is mainly governed by two forces: The gravitational force and the radiation pressure. For my calculations, it is enough to consider the Newtonian gravitational force and not relativistic gravity:

$$F_G = \frac{GM_\star m_p}{r^2} \tag{2.16}$$

$$= \frac{4G\rho\pi R^3 M_\star}{3r^2} \tag{2.17}$$

In Equation 2.17 I assumed the dust particles to be a perfect sphere with a constant density ρ and radius R. r is the distance between the planet and the star, G is the gravitational constant, m_p is the mass of the planet and $M_\star$ is the mass of the star. The force of the radiation pressure is given by:

$$F_r = \frac{L_\star A}{4\pi c r^2} Q_{pr} \tag{2.18}$$

Here $L_\star$ is the luminosity of the star, A is the surface area of the particle, c is the speed of light and Q_{pr} is an efficiency factor. The β-factor is the ratio between the radiation pressure and the gravitational force:

$$\beta = \frac{F_r}{F_G} \tag{2.19}$$

$$= 0.577 \left(\frac{\rho}{g \cdot cm^{-3}}\right)^{-1} \left(\frac{R}{\mu m}\right)^{-1} \left(\frac{L_\star}{L_\odot}\right) \left(\frac{M_\star}{M_\odot}\right)^{-1} \tag{2.20}$$

where R is the particle size and ρ is the particle density. Equation 2.20 is in the units used by Kirchschlager and Wolf [2013] (Eq.10), they assumed Q_{pr} from Equation 2.18 to be one. To calculate the surface area A in the same equation they assumed the particle to be a sphere. From this equation, it is evident that the β-factor becomes larger with a smaller particle size. This means that the gravitational force decreases faster than the radiation pressure with a decrease in particle size. A large particle moves towards the star because the gravitational force is stronger than the radiation pressure. But when it decays, it becomes smaller and it will reach the point where the radiational pressure and the gravitational force are equal. If it continues to decay, the radiational pressure will start to dominate the particle's movement and it starts to move outwards. The size where particles are so small that they leave the system is called "blow-out-size" (Kirchschlager and Wolf [2013]). This size depends on the star's type and the particle's density. This equation is a good estimate for a particle that absorbs all the incoming radiation. I will use this equation for the qualitative analysis in my simulations.

To take the wavelength dependence of the absorption into account, I used another formula by Kimura et al. [2002]:

$$\beta = \frac{\pi R_\star^2}{G M_\star m_p c} \int B_\star(\lambda) C_{pr}(\lambda) d\lambda \tag{2.21}$$

G is the gravitational constant, $R_\star$ and $M_\star$ are the radius and mass of the star, m_p is the mass of the dust, $B_\star(\lambda)$ is the Planck-function of the star and $C_{pr}(\lambda)$ is the radiational pressure cross-section. The radiational pressure cross-section is given as $C_{pr} = C_{abs} + (1 - g_0)C_{sca}$ where C_{abs} and C_{sca} are the absorbtion and scattering cross-sections. g_0 is the asymmetry parameter. It depends on the direction in which the particle is likely to scatter the incoming radiation. This formula depends on the wavelength and takes longer to compute. I will use it for the more accurate simulations.

There are different reasons a particle decays. It can happen due to collisions with other dust particles or by the star's radiation that causes it to attain a high temperature and evaporate. Kobayashi et al. [2011] found the mass-loss rate of a particle due to sublimation to be:

$$-\frac{dm}{dt} = A \sqrt{\frac{\mu m_\mu}{2\pi k_B T}} P_0 \exp\left(-\frac{\mu m_\mu H}{k_B T}\right) \tag{2.22}$$

A is the surface area of the particle, k_B is the Boltzmann constant, T is the temperature, m_μ is the atomic mass unit, μ is the mean molecular weight of the dust material, P_0 is the saturated vapour pressure and H is the latent heat of sublimation.

The reason sublimation exists is that the temperature of the dust particle is the average of the kinetic energy of all the molecules and atoms it is made from. The "escape velocity" in the case of a dust grain is the velocity needed to escape the binding in the inner structure of the dust particle and not its gravitation. Some atoms have a much higher kinetic energy than others, which means that some have the "escape velocity". The atoms, which have the "escape velocity", are the ones that sublimate. Those are necessarily the atoms with more than the average kinetic energy and their escape lowers therefore the average kinetic energy and thereby the temperature of the dust particle.

The change in temperature of the dust particles was by Hans-Peter Gail [2013] described with an energy balance. On one side is the incoming energy, which is the light the star emits (the Planck function for the temperature of the star) multiplied by the absorption cross-section. Since the absorption cross-section depends on the wavelength, it needs to be integrated over the wavelength together with the Planck function. This is scaled by a geometry factor, since the flux changes with the distance from the star. On the other side of the equation is the outgoing radiation. The first part is the Planck function with the temperature of the dust particle multiplied by the cross-section and integrated over all wavelengths and angles. This is the outgoing energy due to the black-body radiation. The second part is the mass loss rate multiplied by the latent heat of sublimation. This is the energy the particle loses due to the sublimation. The formula for this is:

$$\Omega \int C_{abs}(n,x) B_\star(\lambda) d\lambda = 4\pi \int C_{abs}(n,x) B_p(\lambda, T) d\lambda - \frac{dm}{dt} H \tag{2.23}$$

where

$$\Omega = 2\pi \left(1 - \sqrt{1 - \left(\frac{R_\star}{r} \right)^2} \right) \tag{2.24}$$

with $R_\star$ being the radius of the star and r being the distance between the star and the dust particle. $C_{abs}(n,x)$ is the absorption cross-section and its arguments are the complex refractive index n and the size parameter $x = 2\pi a/\lambda$. $B_\star(\lambda)$ is the stellar radiance and $B_p(\lambda, T)$ is the Planck function of the dust particle. Valdés et al. [2023] used this equation in their simulations; I will later compare my simulations with theirs.

The only question left to consider is, whether the particles would have a sufficient velocity to escape the planetary gravitation at all. Those that escape will behave as discussed above, while the others will eventually fall back to the planet or orbit it. Brogi et al. [2012] suggests that outgassing particles would not have the velocity to escape the gravitation of a super-earth. The escape velocity is approximately 23 km/s, which particles do not reach from volcanic activity such as the one on Earth, where the maximal ejection velocity is

2 km/s (Taddeucci et al. [2017]). But on Io, the most volcanically active object in the solar system, such velocities up to 100 km/s are possible (Beckett et al. [2022]). This means that it is only possible for particles to escape the planet's atmosphere if the volcanism is very strong. But it cannot be said with any certainty, since it would highly depend on the interior process leading to the volcanic activity. It is very reasonable to assume that a large amount of dust and larger particles could escape the gravity of the planet if it collides with a moon or if orbital debris from such a collision decays over long timescales.

2.6 Pulsar Planets

Exoplanets do not only exist around stars but may also be found around compact objects such as pulsars. Pulsars are fast-rotating neutron stars that emit synchrotron radiation. They are the remnants of supernovae of massive stars and have masses between 1.4 and 3 solar masses. They are the objects with the highest density without an event horizon. The synchrotron radiation is emitted along the symmetry axis of their magnetic field, which does not align with their spin axis. This means that we cannot see the radiation all the time, we only see it as light flashes or pulses, whenever it is directed towards us. They emit mostly radio waves, but some emit X-rays or optical light as well.

The periodicity of these light pulses is very regular. Wolszczan and Frail [1992] found that one pulsar (PSR B1257+12) had a change in the frequency of its pulses. These changes had a periodicity, which they matched to the existence of two planets with Keplerian orbits around the pulsar. This was the first discovery of planetary mass objects outside the solar system. A third planet was later discovered in the same system (Wolszczan [1994]).

The method with which the pulsar planets were discovered, is similar to the radial velocity method described in Section 2.1. But instead of using the Doppler shift in the wavelength of the emitted light, it used the shift in the time interval between two pulses. The time between the pulses changes if the pulsar moves because the distance one pulse has to travel to the observer changes as the pulsar is moving around the centre of mass due to the gravity of the orbiting planet. This leads to a periodic change in the frequency of the pulse arrivals if a planet orbits the pulsar.

There is some debate about how those planets could form. A planet cannot survive the supernova of its host star (Niţu et al. [2022]). There are planets that escaped another star and that could be captured by a pulsar but that is rather unlikely(Fabian and Podsiadlowski [2003]). This leaves as the only other explanation that there has been a protoplanetary disk around pulsars which have planets.

Currie and Hansen [2007] found by simulating different scenarios that the origin of the material, the planets formed from, can be seen from the architecture of the system. There are two ways, a pulsar can get a protoplanetary disk: The first one is material from the supernova in which the pulsar was formed, which does not have the escape velocity and therefore falls back towards the pulsar. This is called the supernova-fallback. The second

possibility is the tidal disruption of the pulsar's binary companion. The disk material would thereby come from the former companion and not from the pulsar itself. Most of the parameters of the discs, formed in those ways, are close to the parameters in protoplanetary disks around stars. Currie and Hansen [2007] found that the planets formed from the supernova-fallback are mostly orbiting at a distance of less than 1 AU while the planets forming from a disk of tidal disruption tend to be at a distance between 2 and 6 AU. The mass that is available for planet formation in the second case is smaller than in the first. They conclude that the planets belonging to PSR B1257+12 were probably formed from a protoplanetary disk with material from the supernova-fallback.

A recent study (Niţu et al. [2022]) found that there are probably not many pulsars with planets. They took a sample of 800 pulsars and observed only one potential planet. There are certainly no planets much more massive than the Earth around the other pulsars. The signal of a planet smaller than $0.02\,M_\oplus$ could be hidden in the noise of the measurement for most of the pulsars. This shows how unique the PSR B1257+12 system is. Since the lightest planet detected in the system has a mass of $0.02\,M_\oplus$, there is the possibility for small masses to be detected in this system. It is therefore reasonable to ask if exomoons could likewise be detected. This is one of the questions I will try to answer in this thesis.

All three planets are within 0.5 AU, which makes it a compact system. As discussed in Section 2.3 a moon in such a system would have to be within half the Hill radius (Equation 2.14) to be on a stable orbit. The Hill radius of the Earth is $1.4714 \cdot 10^6$ km, and the distance of the moon is $3.84400 \cdot 10^5$ km and thereby well within half the Hill radius. If we now compare that to the Hill radii of the planets B and C around the pulsar PSR B1257+12, which are for planet B $7.83 \cdot 10^5$ km and for planet C $9.68 \cdot 10^5$ km, it is obvious that a moon within half that distance could not have a long orbiting time (the maximum is about ten days), even though they are both heavier than the Earth (see Table 3.3). The reason for this is that they are much closer to the pulsar than the Earth is to the sun. This makes the gravitational field of a planet in comparison with that of its central object smaller.

The Roche radius cannot be exactly calculated since all three parameters in Equation 2.15 are unknown (radius of the planet and densities of the planet and the moon). The pulsar has a luminosity of $5.2\,L_\odot$ (Josette Wright and Wang [2006]) and the planets are within 0.5 AU, it is therefore very likely that they are not icy planets and with masses of less than $5\,M_\oplus$ they are no gas giants. They are therefore probably rocky planets and their moons are probably rocky as well. This means that the quotient of their density is between 0.5 and 2. The Roche radius is therefore probably not much larger than 1.25 times the planetary radius. The planetary radius will probably not be more than an order of magnitude larger than that of the Earth. This means that a moon at a distance of 10^5 km is certainly outside of the Roche radius.

3 Method

After having discussed the foundational concepts above, I will move on to describing my methodology. I will start with an explanation of why we need to do the simulations with an N-body simulation. I will afterwards describe the program I wrote to simulate the TTVs of 55 Cnc e and test it on WASP-47 with a short discussion of the problems that typically occur when simulating TTV's. I will then move on to a description of the simulation of the dust particles and a test by comparing it to results found by Valdés et al. [2023]. In the last part of this section, I will describe my model to simulate the pulse timing variations and test it by reproducing the signal of the discovery of the planets around this pulsar.

3.1 N-body simulations

It is impossible to solve the gravitational equations for the behaviour of planetary systems with more than two bodies (i.e. more than one planet). The three-body problem can be solved in special cases such as one particle being assumed to be a test particle with neglectable mass (the "restricted" case) or the one where two particles have a mass much smaller than the third ("Hill's case"). But since all the systems I look at, have at least three planets, no such approximation can be helpful. In such cases, the equations have to be solved numerically. This is the purpose of an N-body simulation. I use a Python package called "Rebound" Rein and Liu [2012] to simulate planetary systems in an N-body simulation.

The most important part of this simulation is the integrator. The integrator that I will be using throughout this thesis is called IAS15 (Integrator with Adaptive Step-size control, 15th order)(Rein and Spiegel [2014]). The basis of the integrator is the Gauß-Radau quadrature. This is a generalisation of the Gauß-quadrature (Eyre and Miller [1990]). The Gauß-quadrature is an approximation for an integral with the sum over a polynomial, which was first proposed by Gauß [1815] and shortly afterwards modified by Jacobi [1826]. The resulting formula is:

$$\int_a^b f(x)dx \approx \sum_{i=1}^{n} f(x_i)\alpha_i \tag{3.1}$$

Where $f(x)$ is the function to be integrated, x_i are the "nodes", points of evaluation of the function and α_i are weights for the sum. The nodes are chosen to be the zeros of the nth "orthogonal polynomial". The orthogonal polynomials are an infinite sequence of polynomials, which are orthogonal to each other (Milton Abramowitz [1965]). The Gauß-quadrature is an exact solution for the integral if $f(x)$ is a polynomial of degree $2n-1$ or less. If $f(x)$ is not a polynomial, there has to be the possibility to write it as $f(x) = \Phi(x) \cdot \omega(x)$ where $\Phi(x)$ is a polynomial, which can be integrated exactly and $\omega(x)$ is a weight function, in order to use this theorem. In this case, the approximation cannot

be exact and it becomes:

$$\int_a^b f(x)dx = \int_a^b \Phi(x)\omega(x)dx \approx \sum_{i=1}^{n} \Phi(x_i)\alpha_i \tag{3.2}$$

The Radau quadrature is a generalisation of the Gauß quadrature (Radau [1880]), which can be written as

$$\int_{-1}^{1} f(x)dx \approx \alpha_1 f(-1) + \sum_{i=2}^{n} \Phi(x_i)\alpha_i. \tag{3.3}$$

It is accurate up to a degree of 2n (Hildebrand [1956]). Another difference between the Gauß-quadrature and the Gauß-Randau-quadrature is that the Gauß-Randau-quadrature includes the starting point of the integral as one of the nodes.

The IAS15 integrator uses an approximation for the acceleration as the starting point, which is integrated to get the velocities and positions. The acceleration is approximated by a polynomial of degree 7, which has time as the free parameter. The positions and velocities are approximated in timesteps dt. Each timestep is divided into sub-steps, which are spaced like the nodes of the Gauß-Randau-quadrature.

The approximation is done in a predictor-corrector loop: It begins with an estimate of the positions and velocities, from which it calculates the force (in the first iteration the force is assumed to be constant). This force is then used to calculate more accurate positions and velocities. This is repeated until the positions and velocities converge. In every timestep except the first one, the change of the force in the previous timestep is used to make a better prediction of the force in the next step. Which leads to a small number of iterations in the predictor-corector loop. For everything I explained so far, the size of the timestep is fixed. But if the predictor-corrector loop cannot find a converging result after twelve iterations, the process is cancelled, the stepsize becomes smaller and the loop starts new.

This means that the integrator can adapt to a change in the time scale in which the force changes in the system and still integrate to machine precision. This makes it fast (because in most cases only a few iterations in the predictor-corrector loop are necessary) and exact. This is the reason, I chose to use this integrator for my simulations.

3.2 Transit timing variation/WASP-47

I ultimately aim to use an N-body integration to simulate the TTVs of 55 Cnc e. However, I will first describe how the program measures the timing of a transit event and then use the example of the WASP-47 system which has known TTVs, to validate my code and to explain some difficulties that arise when modelling TTVs.

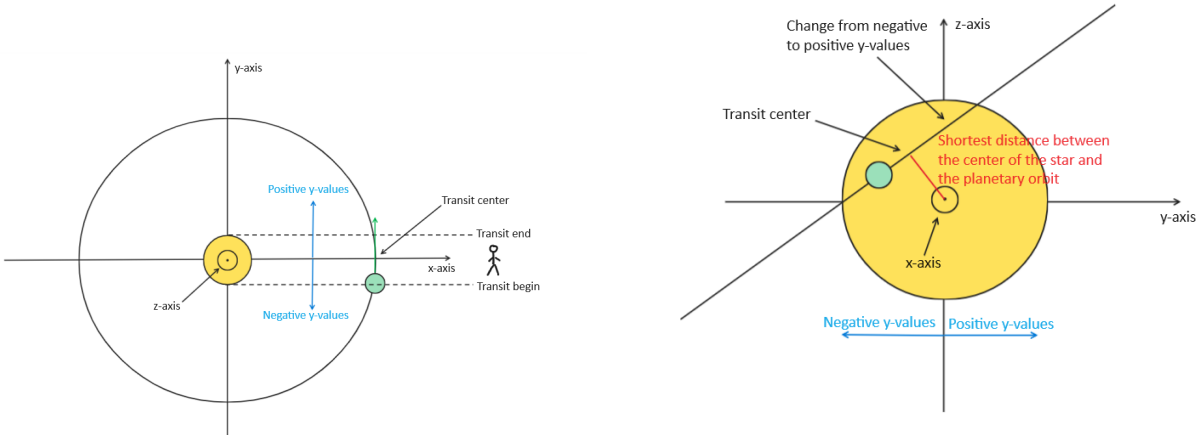

(a) Transit seen face on

(b) Transit seen edge on

Figure 3.1: Fig. 3.1a shows a star and its planet at the beginning of the transit. The planetary orbit is in the x-y-plane. The observer is on the positive end of the x-axis, and the transit center is at the change from negative to positive y-values. Fig. 3.1b shows the transit of a planet with an orbit not in the x-y-plane. The center of the transit is therefore not at the change from negative to positive y-values but at the shortest distance between the center of the star and the planetary orbit in the y-z-plane.

3.2.1 The model for TTVs

For the transit timing variations, I set the observer on the positive end of the x-axis while the star started close to the origin. I started from the method by Rein and Winkler [2021] where the transit is determined by the change of sign in the y-coordinate combined with a positive x-coordinate (Fig. 3.1a). This, however, does not always give the transit center time, which is the time of the smallest distance between the center of the star and the center of the planet in the y-z-plane as shown in Fig. 3.1b. I wrote a code such that it is looking for this distance. This is done by comparing the distance between the previous and the latest integration with integration time steps of 0.1 seconds. After finding the shortest distance, I saved the time and the position of the planet, which is the transit, integrated over 99% of the orbit then saved the position of the planet and repeated the process. Integrating over 99% of the orbit before the program starts to look for a transit prevents the program from mistaking a secondary eclipse as a transit.

The units the program uses are such that the mass of the star is one, the distance between one chosen planet and the star is one and the orbiting period of this planet is 2π. To transform the results into more intuitive units, I used for 55 Cnc e that the orbiting period of planet e is 0.7365474 days (Zhao et al. [2022]). The code of my model is in the Appendix A.

	Mass	Distance from the star	Eccentricity	Inclination
Star	$1.040\,M_\odot$			
Planet e	$6.83\,M_\oplus$	0.01695 AU	0.0	85.98°
Planet b	$363.1\,M_\oplus$	0.05130 AU	0.0	88.98°
Planet d	$13.1\,M_\oplus$	0.086018 AU	0.0	89.32°
Planet c	$398.2\,M_\oplus$	1.393 AU	0.296	90°

Table 3.1: Parameters used to simulate WASP-47. The parameters are all taken from Vanderburg et al. [2017], excepting the inclination of planet c and the eccentricity of planets e and b, which are unknown, so I had to assume values. For planet c the mass is the minimum mass. Planet e has been discovered by the transit method by Becker et al. [2015] and has been confirmed with the radial velocity method by Vanderburg et al. [2017]. It has been first discovered by Hellier et al. [2012]. Planet c and d were discovered by the radial velocity method by Neveu-VanMalle et al. [2016].

3.2.2 Tests on WASP-47

Let us now move on to testing this code by simulating the transit timing variations of the system WASP-47. WASP-47 is a system with four planets of which the three inner planets are transiting. The parameters of this system are shown in Table 3.1.

In this system, planets b and d have a transit timing variation which Vanderburg et al. [2017] found to be of about 0.8 and 8 minutes respectively. I could reproduce the result with my simulations as can be seen in Fig 3.2 but not very exact. Planet e does not have any measurable TTVs, which my simulation reproduced (Fig. 3.2a). The measurements by Vanderburg et al. [2017] (in my figure the green dots) are a bit scattered but with such error bars that my simulation (the purple dots) is lying well in the possible range and very close to the simulation of Vanderburg et al. [2017] (the red dots).

The initial alignment of the planets can be obtained from the paper Vanderburg et al. [2017] in the form of the exact time of the first (in the paper used) transit of each of the planets. If I initialize my model to start at exactly the time of the first transit, then this transit would have a timing variation of zero, because it is by the initial conditions fixed at this time and therefore occurs at exactly the expected time. This means that a burn-in time is needed, which is the amount of time between the start of the simulation and the first of the transits shown in the paper. Vanderburg et al. [2017] also used a burn-in time, but since they only mentioned the number of time steps during this time and not the length of those steps, it was not possible to use the same length. I chose 70 orbital periods of planet b (which corresponds to 291 days and 32 orbital periods of planet d) as my burn-in time.

The second thing to consider is the way of calculating the TTVs. The program (as described above) gives the timing of each transit, but in order to get the TTVs those timings must be compared to the expected timing. This expected timing is the number of transits n

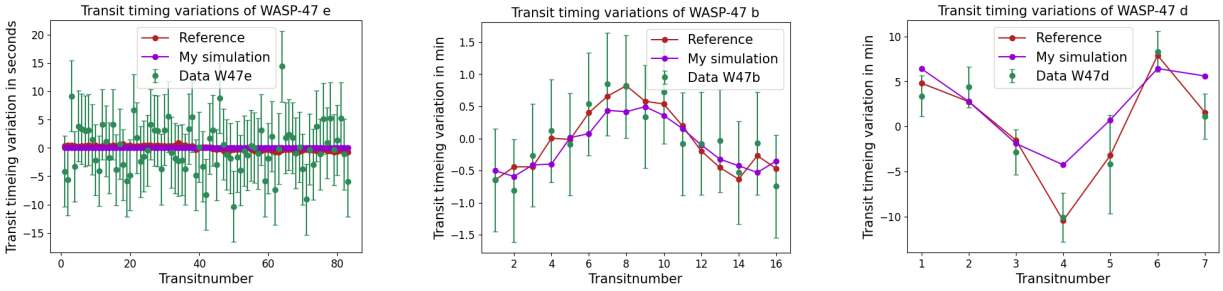

(a) Planet e (b) Planet b (c) Planet d

Figure 3.2: The figure shows the transit timing variation of the WASP-47 system. The green dots represent the measured data and the red dots represent the TTVfast simulation from Fig. 1 in Weiss et al. [2017]. I extracted the data from the picture using the "WebPlotDigitizer" (`https://automeris.io/WebPlotDigitizer/`) made by Ankit Rohatgi in 2010. The purple points represent my own simulation. I used a burn-in time of approximately 291 days, which corresponds to 395 periods for planet e (Fig. 3.2a), 70 periods for planet b (Fig. 3.2b) and 32 periods for planet d (Fig. 3.2c).

times the orbital period P. If we call the expected timing t_e and the actual timing t_a, we get $t_e = n \cdot P$ and the transit timing variation (TTV) is $TTV = t_a - t_e = t_a - nP$. The orbital period is the average over many transits. The problem is that the TTVs follow a periodicity with several different frequencies as can be seen in Fig. 3.3 on the example of planet d. In Fig. 3.3a is the longest of the changes in the TTVs visible with a periodicity of about 2000 transits. Fig. 3.3b shows a zoomed-in picture of the first 800 transits and Fig. 3.3c even more zoomed-in on the first 49 transits. In each of those plots, I used the averaging interval equal to the number of transits shown in the respective plot. It is clearly visible by comparing Fig. 3.3a and Fig. 3.3b that the amplitude and (to a smaller extent) the shape of the TTV-curve depend on the number of transits the average period is calculated with. This could account for some part of the difference between my simulation and the simulation done by Vanderburg et al. [2017] (Fig. 3.2).

One possible reason for the deviation of my simulation from the results in Vanderburg et al. [2017] is a difference in the parameters (burn-in time and number of periods to average over). I, therefore, calculated the TTVs for many different burn-in times and different numbers of periods to average over. The results varied but a long burn-in time generally produced worse results. This can be explained by the fact that the period changes significantly over the course of a few hundred periods, but the calculation is done with one fixed period as a reference, leading to an offset. Another difference is the use of a different integrator and their algorithm to avoid the summing up of numerical errors described in Deck et al. [2014]. Implementing both did not visibly change the results.

To understand the computational noise of the simulation, I did the transit timing simulation of 55 Cnc with only the planets e and b, assuming they were massless. I did the simulation

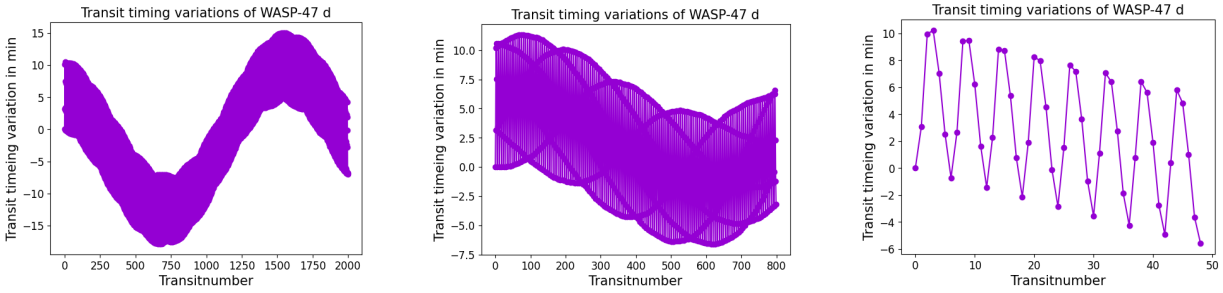

(a) First 2000 transits (b) First 800 transits (c) First 49 transits

Figure 3.3: The figure shows the transit timing variation of WASP-47 d. The different plots show different numbers of transits, starting with the same initial conditions (32 burn-in periods). The number of periods, over which was averaged for the expected arrival of the transits, is always the same as the number of transits plotted in each plot.

20 times with different initial conditions and subtracted from each transit time the one of the transit before. I then calculated the standard deviation, which was $3.3 \cdot 10^{-4}$ s. This means that the uncertainty due to the fact that the model calculates the transit with an accuracy of 0.1 seconds is much larger than the computational noise.

The conclusion from those considerations is that my program is able to reproduce the qualitative shape of the TTVs of WASP-47. The amplitude is not exactly reproduced but very close and for most of the data points within the standard deviation. Some part of the deviation from the result can be explained by different parameters (burn-in time and the number of transits that are averaged to get the period). However, it is unlikely that a summing up of numerical errors or the computational noise is a large source of error.

3.3 Dust particles

I will now discuss the model which simulates dust particles. The goal is to determine the lifetime, size and temperature of those particles as well as their trajectory to see if they could be responsible for the variation in the occultation depth that was observed for 55 Cnc e.

The model is based on the Python library "Rebound", as well as the library "Reboundx" to implement the radiational pressure (Tamayo et al. [2019]). After implementing the planetary system with the parameters from Table 3.2, I added the dust particles, assuming them to be massless particles. To test, if the program was principally working, I made a test simulation, where the model emitted 500 dust particles five times over a simulation time of ten hours. I distributed the particles randomly around the planet and gave them a starting velocity randomly distributed around the escape velocity pointing in a randomly chosen direction within the semisphere pointing away from the planet. The dust formed a

	Mass	Semi-major axis	Eccentricity
Star A	$0.92\,M_\odot$ [1]		
Planet e	$7.99\,M_\oplus$ [2]	$0.015\,\mathrm{AU}$ [3]	0.023 [5]
Planet b	$0.84\,M_{Jupiter}$ [4]	$0.11\,\mathrm{AU}$ [4]	0.0023 [5]
Planet c	$0.178\,M_{Jupiter}$ [5]	$0.237\,\mathrm{AU}$ [5]	0.072 [5]
Planet f	$0.148\,M_{Jupiter}$ [5]	$0.773\,\mathrm{AU}$ [5]	0.08 [5]
Planet d	$3.84\,M_{Jupiter}$ [6]	$5.4\,\mathrm{AU}$ [5]	0.027 [5]
Star B	$0.264\,M_\odot$ [7]	$1050\,\mathrm{AU}$ [8]	0.0

Table 3.2: The table shows the parameters I used for the simulation for 55 Cnc. The masses are the minimum masses (see Section 2.1) only the masses for the star and planet e are the actual masses and not the minimum masses. I assumed the eccentricity of star B to be zero because it is unknown and its effect is small due to the large distance. I simulated the TTVs with many different parameters for the longitude of the ascending node and inclination. I used a step size of 0.1 rad (approximately 5.7°) for the longitude of the ascending node and 0.02 rad (1.1°) for the inclination, assuming star B and all planets except planet e to orbit in the same plane. I motivate this in Section 4.1.

cloud at the distance of the planet around the star. The behaviour of the dust particles did not change significantly if they were massive (i.e. gravitationally interacting with each other), but it slowed the simulation down. I did therefore all the following simulations with massless particles.

I then proceeded to add a finite lifetime to the dust particles. For this, I initialised the grain size randomly following a uniform distribution and assumed a constant density i.e. a uniform composition. I then assumed the dust particles to be perfect spheres and used Eq. 2.22 to calculate the change in radius from the mass-loss and thereby the change in the β-factor. I remove the particles if their radius is below $0.001\,\mu$m. I simulated dust particles made of carbon (graphite). Valdés et al. [2023] simulated several different materials and carbon showed both a long lifetime and a strong dependence between grain size and lifetime, which made it interesting. I planned to simulate other materials afterwards but ran out of time. There are different parameters: Kobayashi et al. [2011] uses a density of $1.95\,\mathrm{g/m^3}$, a molecular weight of 12.0 a latent heat of sublimation of $7.27 \cdot 10^{11}\,\mathrm{erg/g}$ and a saturated vapour pressure of $4.31 \cdot 10^{16}\,\mathrm{dyn/cm^2}$. Valdés et al. [2023] used for their simulations the parameters found by van Lieshout et al. [2014]. They used for the density $2.16\,\mathrm{g/cm^3}$, for the molecular weight of 12.0, for the latent heat of sublimation $\exp(36.7)\,\mathrm{dyn/cm^2} = 8.68 \cdot$

[1] The value is from Fischer et al. [2008]
[2] The value is from Zhao et al. [2022]
[3] The value is from Bourrier, Vincent and Hébrard, Guillaume [2014]
[4] The value is from Butler et al. [1997]
[5] The value is from Nelson et al. [2014]
[6] The value is from Zandt et al. [2023]
[7] The value is from Schweitzer et al. [2019]
[8] The value is from Raghavan et al. [2006]

10^{15} dyn/cm^2 and for the saturated vapour pressure $6.48{\cdot}10^7$ J/kg $= 6.48{\cdot}10^{11}$ erg/g. Those sets of parameters are within the standard deviation of each other. I did the simulation with both and there was no visible difference. I will use the parameters used by Valdés et al. [2023] to be later able to compare my results to theirs.

Using the energy balance (Eq. 2.23) requires a cross-section and the radial pressure (Eq. 2.21) needs the asymmetry factor. I used a program called LX-MIE Kitzmann and Heng [2017] to calculate them for carbon. LX-MIE takes as free parameters the radius of a particle, its composition, and its (pre-tabulated) complex refractive index, and calculates the absorption and scattering cross-sections and the asymmetry parameters. To speed my simulations up, I calculated the cross-sections and the asymmetry parameters once before and tabulated them. When the program runs I therefore only call the tabulated values. I used a step size of $0.001\,\mu$m between $0.001\,\mu$m and $10\,\mu$m. To avoid jumps in the change of $\frac{dm}{dt}$ and the temperature, I linearly interpolate between the cross-sections to get a continuum for different radii. I do that by determining the closest radius for which I calculated the cross-section. If the radius is exactly equal to the particle's radius, I take that cross-section. Suppose the particle's radius is unequal to the pre-tabulated radius. In that case, I take the cross-section for the next smaller or larger radius that I tabulated such that $R_1 < R_{dust} < R_2$ where R_1 and R_2 are the two closest radii in the table with their corresponding cross-sections C_1 and C_2. The cross-section decreases with a decrease in the radius. I interpolate between the cross-sections by using

$$C_{dust} = (C_2 - C_1) \cdot \frac{R_{dust} - R_1}{R_2 - R_1} + C_1. \tag{3.4}$$

I do the same with the asymmetry parameter from Equation 2.21.

The model takes as free parameters the duration of the simulation and the number of evaluation points. The time between the points is equally spaced. The mass of the particles and their radius are related by assuming them to be perfect spheres with a constant density. After initialising the system, the simulation works as follows:

1. Simulate until the next evaluation point (the first one is always at $t = 0$)
2. Save the positions, velocities, radii and calculate and save the β-factors for all of the dust particles
3. Calculate and save the temperature by solving Eq. 2.23 with scipy.optimize.fsolve and numpy.trapz
4. Calculate the mass loss rate and use it to calculate the new mass from which it calculates the new radius
5. Remove the particle, if the radius is smaller than $0.001\,\mu$m
6. Save the position of the star and the planets e and b

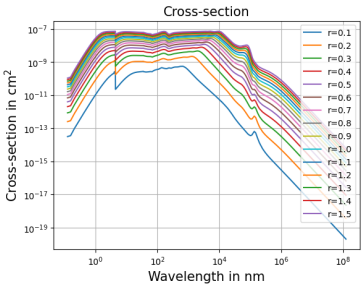

(a) Cross-sections for different particle sizes

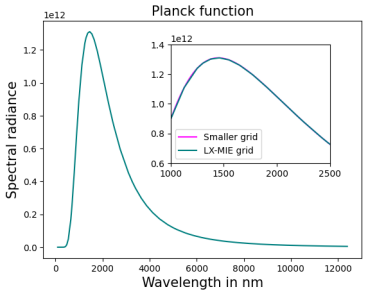

(b) Planck function with the grid of the wavelength' (zoomed-in)

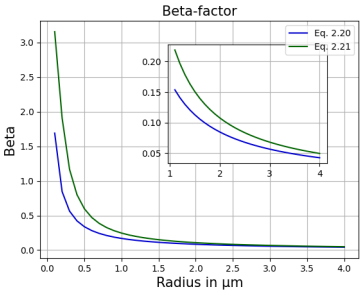

(c) β-factor calculated with equations 2.20 and 2.21

Figure 3.4: Fig. 3.4a shows the cross-sections of carbon calculated with LX-MIE for different particle sizes as a function of the wavelength, the radii given in the legend are in μm. It is clearly visible that the cross-sections change smoothly with a small change in radius. Fig. 3.4b shows the Planck function for 2000 K as a function of the wavelength. The points at which the function is evaluated are all points at which the cross-section is calculated by LX-MIE. The part shown in this plot is a zoomed-in version of the only part, in which the function changes fast. The part in the sub-figure is even more zoomed-in. In the wavelength grid of LX-MIE are only 15 points in the interval 1000-2500 nm. The magenta curve is the function but with a ten times smaller grid and there is almost no difference visible. Fig. 3.4c shows the beta-factor calculated with Equation 2.20 (blue) and with Equation 2.21 (green). The inset shows a zoomed-in version.

If dust was emitted at several different times into the system, it would be done in between two iterations of the loop described above. The simulation would continue afterwards as before. The code of my model is in Appendix B.

To test this part of my code, I let it run for just one particle at a fixed distance (equal to the semi-major axis of planet e) from the star and for different particle sizes for an hour with 1000 time steps. All dust particles larger than 0.4 μm survived the one hour. The decrease of the particle's radius was very slow for larger grains. I therefore decided to simulate only particles with a radius smaller than 5 μm.

LX-MIE approximates the cross-sections not as a smooth function but as a table with a grid of wavelength and their corresponding cross-sections. This means that the integrator can only evaluate the integral of the product between the cross-section and the Planck function at the points of the grid of Wavelength given by LX-MIE. To see if the grid samples the Planck function fine enough, I plotted the function using the grid points. For a small area around the peak, I also plotted the function using a ten times smaller grid. This is shown in Fig. 3.4b. The part that is shown in the plot does not include the whole wavelength range but only the part where the Planck function changes significantly. The Planck function for the wavelengths smaller than 95 nm the exponential in the denominator becomes so large

	Planet A	Planet B	Planet C
Mass	$0.02\,M_\oplus$	$4.3\,M_\oplus$	$3.9\,M_\oplus$
Period	25.262 days	66.5419 days	98.2114 days

Table 3.3: This is the naming convention I used for the pulsar PSR B1257+12 and its planets. The parameters are taken from Konacki and Wolszczan [2003].

that this part is neglectable. It is clearly visible from this plot that the grid is small enough to evaluate the function accurately since a smaller grid does not significantly change the shape of the curve. Fig. 3.4a shows the cross-sections of carbon for all wavelengths in the grid for different particle sizes, the radii are given in the legend in units of μm. It is visible that the cross-sections change smoothly with small changes in the particle size for particles larger than $0.5\,\mu$m, there are no jumps from one line to the next. The change increases when the particles become smaller.

There are two different ways to calculate the beta-factor (the ratio between the radiation pressure and the gravitational force), as discussed in Section 2.5.2. One of them (Equation 2.20) neglects the wavelength dependence of the absorption and assumes no preferred direction for reemitting radiation. Equation 2.23 takes both into account but takes longer to compute. Fig. 3.4c shows the beta-factor calculated with both equations as a function of the particle radius. The difference is small for large particles but it increases the smaller the particles become. I will use Equation 2.23 because the radiation pressure is most important for smaller particles.

3.4 Pulsar planets

In this section, I will describe how I simulate the effect planets (or their moons) orbiting a pulsar would have on its movement. To make a simulation that is useful to predict that (see Section 2.6) I have to simulate the movement of the pulsar due to the gravitation of the planets. There are several different naming conventions for those exoplanets and the pulsar. The names of the planets and their parameters are shown in Table 3.3. After importing the parameters as listed in the table, I saved the radial position of the pulsar and then subtracted from each position the first one. By this, I got the distance the pulsar moved since the first timestep. By dividing this by the speed of light, I got the difference in arrival time. This difference is not the difference in arrival time between any two following pulses. It is the difference between the arrival time of the N-th pulse and the time that would have been expected, if, after the first pulse in the simulation, all other pulses were coming at exactly the expected time (if the pulsar did not move).

To test the program, I reproduced the variations in the arrival time of the pulses, that led to the discovery of the planets around PSR B1257+12 (Wolszczan and Frail [1992], Wolszczan [1994]). My results are shown in Fig. 3.5. They are the same as the pulse arrival timing from the discovery papers Wolszczan and Frail [1992] and Wolszczan [1994].

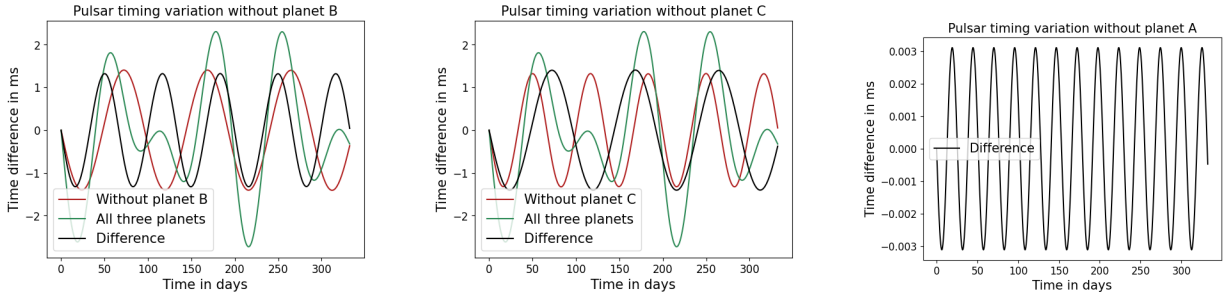

(a) (b) (c)

Figure 3.5: The arrival time of the pulses from PSR B1257+12 compared to the expected arrival time as a function of time. Fig. 3.5a and Fig. 3.5b show the simulated difference in the pulse arriving time of all three planets in green, the simulation, if there were only the two other planets, in red and the difference (the contribution of the planet in question) in black. Fig. 3.5c shows only the difference, since its contribution is much smaller than that of the other two, that it would not be visible if plotted in the same diagram as the others.

When simulating the change in the pulse arrival timing for moons around the pulsar planets, it is important to fix a minimum amplitude the change in arrival timing must have to be detectable. There is no general rule since it highly depends on the pulsar (Niţu et al. [2022]). The error bars on the measurements for even one specific pulsar are different for each data point. I will for the discussion of this pulsar assume the order of magnitude in the signal of planet A as the minimum signal since it can definitely be detected in the case of this pulsar.

The next thing to consider is the influence of N-body interactions on the pulse arrival timing. This means that there is a difference between the pulse timing of the three planets independently added up and that from an N-body interaction of those planets and the pulsar. The difference in the pulse timing of those two cases is shown in Fig. 3.6. By comparing Fig. 3.6 and Fig. 3.5 it is clear that the full N-body simulation diverges completely from the simulation of the three planets modelled independently of one another and added up at the end.

The large influence of the N-body interaction on the pulse arrival timing makes it not immediately intuitive, why the difference between a simulation with all three planets and a simulation with only two planets has a sinusoidal shape (Fig. 3.5). The reason for this is that in Fig. 3.5 the pulse arrival timing has been simulated for a short time. In Fig. 3.7 the same simulations are run for longer times for planets B and C. It is visible that, though the pulse timing variation starts as a sinusoid, there is an amplitude modulation later on, which comes from the N-body interaction. For planet C (Fig. 3.7b) it comes even later than for planet B (Fig. 3.7a), which can be explained with the longer orbiting time of planet C.

To simulate the effect of a moon, which one of the planets might have, it is necessary to

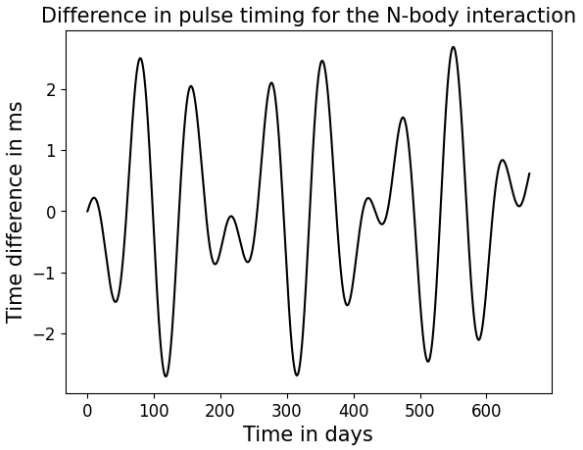

(a) Influence of the N-body interaction (short)

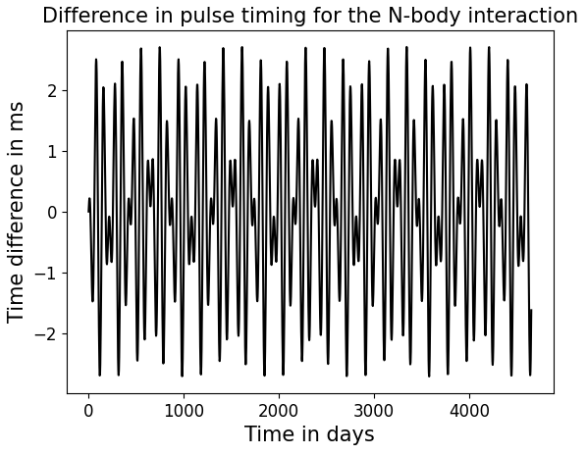

(b) Influence of the N-body interaction (long)

Figure 3.6: The plots show the difference in the pulse arriving between the N-body simulation with all three planets and the added effect of each planet alone depending on time. Fig. 3.6a shows that the effect of the N-body interaction greatly varies over time and that the amplitude is larger than that of the effect of any planet on its own (Fig. 3.5). Fig. 3.6b shows that this does not change materially over a longer timescale.

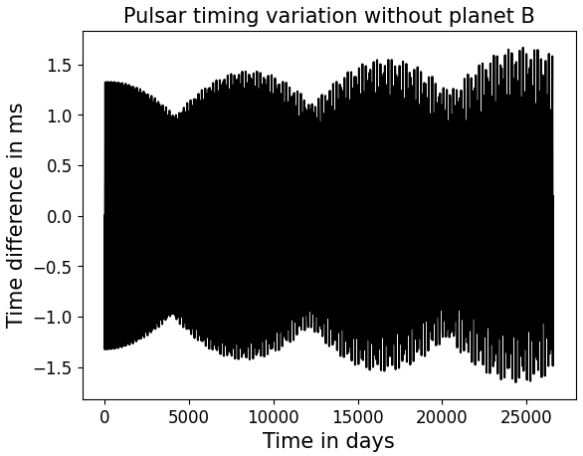

(a) Pulse timing effect of planet B (long)

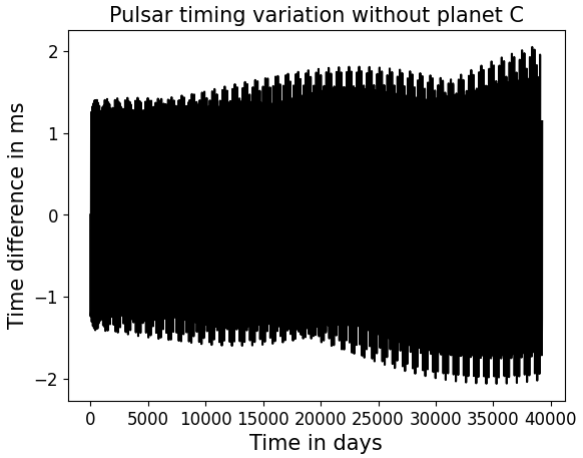

(b) Pulse timing effect of planet C (long)

Figure 3.7: The difference in the pulse arriving time between the simulation with all three planets and one without planet B (Fig. 3.7a) or planet C (Fig. 3.7b) over time. It is visible that over longer timescales the difference is no longer a sinusoid, but the signal has an amplitude modulation, which comes for planet B earlier than for planet C. This is not surprising, since planet C has a longer orbiting period. This shows the effect of the N-body interaction.

Host planet	Moon mass in M_E	Distance in km	Orbiting time in days
B	0.01	10^5	1.76
	0.1	10^5	1.78
	1	10^5	2.01
	0.01	$3 \cdot 10^5$	9.14
	0.1	$3 \cdot 10^5$	9.24
	1	$3 \cdot 10^5$	10.12
C	0.01	10^5	1.85
	0.1	10^5	1.87
	1	10^5	2.14
	0.01	$3 \cdot 10^5$	9.60
	0.1	$3 \cdot 10^5$	9.71
	1	$3 \cdot 10^5$	11.11

Table 3.4: The different parameters used to simulate the moons around the pulsar (PSR B1257+12) planets B and C.

determine the parameters of such a moon. I only added one moon at a time. The moon has to be within half the Hill radius of the host planet as discussed in Section 2.3. I chose distances of more than 10^5 km because the moon is at that distance certainly not within the Roche radius as discussed at the end of Section 2.6. The orbiting times of the moons vary slightly depending on the mass of the moon. This comes from the fact that to avoid adding mass to the system, I decided to subtract the mass of the moon from the mass of its host planet. This means that the mass of the planet varies with the mass of the moon and the change in the planet's mass is responsible for the small change in the orbiting period.

4 Results/Discussion

After describing the methods I used to simulate the TTVs, the dust particles and the pulse timing variations, I will now discuss the results.

4.1 Transit timing variation/55 Cnc

I simulated the TTVs of 55 Cnc e as I described in Section 3.2.1. To simulate the planets of 55 Cnc I used the parameters in Table 3.2.

The transit timing variations of 55 Cnc e are, if we assume all planets to be at an inclination of 55 degrees with the orbital plane of the transiting planet e, on the order of one second as can be seen in Fig. 4.1a where the transit timing variation is plotted as a function of the transit number. The transit timing variation was calculated by averaging over all the transits to get the mean period and then subtracting the expected time (meaning the

period times the number of the transit) from the time of this transit.

As explained in section 2.1 the masses of the planets detected with the radial velocity method depend on their inclination. It is therefore expected that the TTVs of planet e also depend on the inclination of the other planets since the gravitational force will change with the mass, as discussed in Section 2.4. The longitude of the ascending node might also influence the TTVs since it will change when the planets are closest to each other. To investigate this I carried the simulation out with a step size of 0.1 rad (approximately 5.7°) for the longitude of the ascending node and 0.02 rad (1.1°) for the inclination, assuming star B and all planets except planet e to orbit in the same plane. The step size for the inclination is smaller because it is expected to have a larger influence. I calculated the standard deviation, the minimum-to-maximum distance and the mean absolute deviation (MAD) of the TTVs for each of the simulations. All three gave qualitatively the same result, so I will only discuss one of them (the standard deviation), which is shown in Fig. 4.1b. In Fig. 4.1a only 2000 transits are shown to make the single points distinguishable but for Fig. 4.1b I used 5000 transits for each point in the grid.

It is clearly visible that the longitude of the ascending node has a very small influence on the TTVs, as would be expected, since the different timing of the closest approach of the planets might change the exact form of the TTVs, but not the order of magnitude. But it is visible that the TTVs are smaller if the point of closest approach is 45° away from the point of transit. The inclination does not change the TTVs very much except the angles close to 0°. But it decreases rapidly within 5° such that the non-detection of transit timing variations around planet e can put only very small constraints on the inclination of the other planets and thereby on their masses.

4.2 Dust particles

The other question I will address about the 55 Cnc system is the varying occultation depth of planet e. The goal is to get an upper estimate of how long the particles live and how far away from the planet they might reflect a large amount of light. This reflected light could then explain the change in the occultation depth as discussed in Section 2.5. I simulated dust particles with starting radii between 0.1 μm and 4 μm.

Let us first look at the decrease of the radius for a stationary particle which is almost linear most of the time as can be seen in Fig. 4.2c. The particle starts to decay much faster, when it is smaller than 0.4 μm, which matches the result in Fig. 4.3a. The reason for this fast decrease is the increase of the mass-loss rate normalised by the particle's mass (Fig. 4.2a). The absolute mass-loss rate decreases (Fig. 4.2b), but the particle loses a larger part of its mass, which leads to a faster decrease in radius.

Let us now look at the temperature of dust particles. The only parameters that influence the temperature of the dust are the grain size (and by that the cross-section, which depends on the grain size) and the distance to the star. Fig. 4.3a shows the temperature of dust

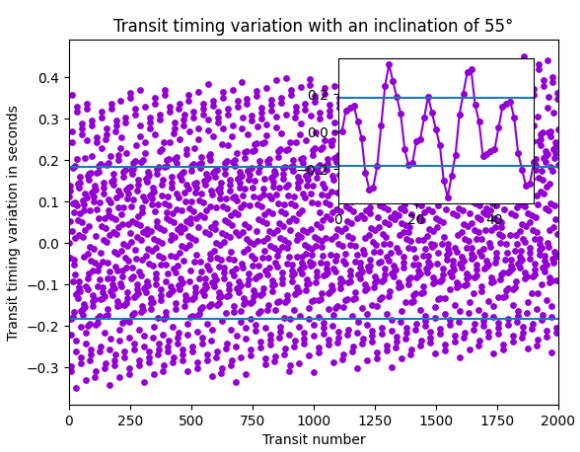

(a) TTVs of 55 Cnc e

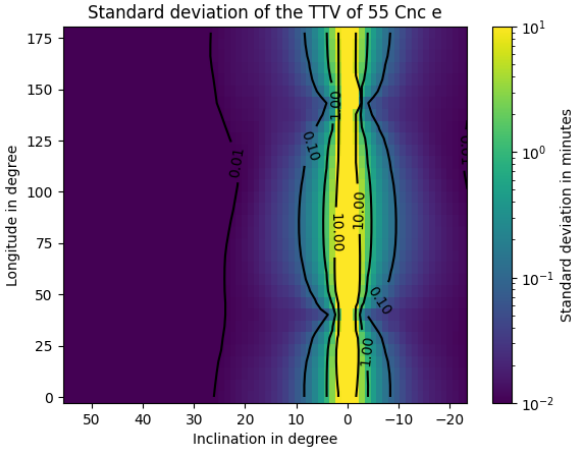

(b) Standard variation of the TTVs of 55 Cnc e

Figure 4.1: The figure shows the transit timing variation of 55 Cnc e. In Fig. 4.1a all the other planets in the system are assumed to have a longitude of the ascending node of 0° and an inclination of 55°. Each point has an error of ±0.1 s. Here are only the first 2000 of the 5000 transits plotted. In the zoomed-in part, where the first 50 transits are visible, one can see a periodic pattern. Fig. 4.1b shows the standard deviation of the transit timing variation in minutes as a function of the longitude of the ascending node and the inclination of the other planets.

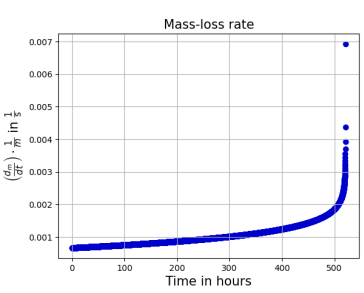

(a) Mass-loss rate normalized by the particles mass over time

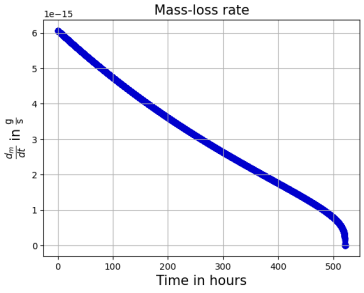

(b) Mass-loss rate not normalized over time

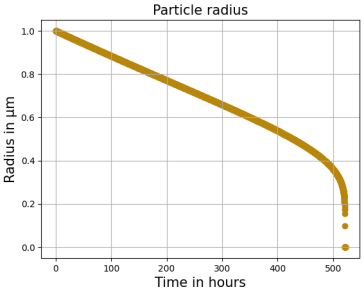

(c) Change of radius over time

Figure 4.2: Figure 4.2a shows the mass-loss rate normalised to the particle's mass as a function of time for a particle with radius 1 μm and a distance from the star of the semi-major axis of planet e. It increases at the end because the particle's mass decreases, as shown in Fig. 4.2b. Figure 4.2c shows the particle's radius as a function of time.

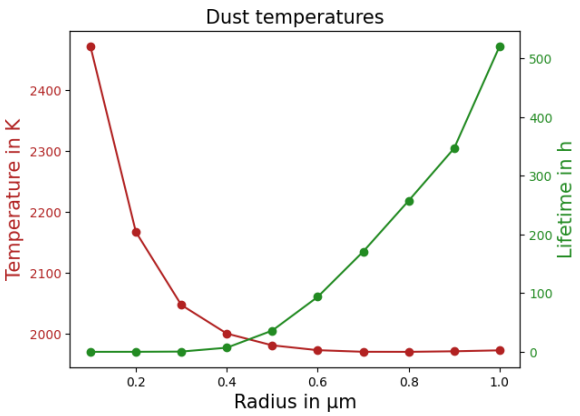

(a) Temperature as a function of radius

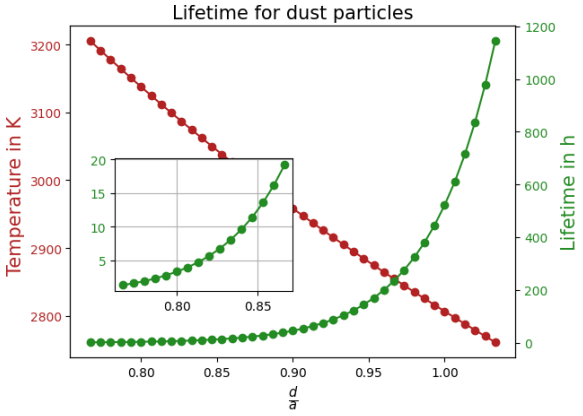

(b) Lifetime as a function of distance between star and particle

Figure 4.3: Fig. 4.3a shows the temperature and lifetime of dust particles at the distance equal to planet e's semimajor axis (0.015 AU) as a function of particle size. Fig. 4.3b shows the lifetime and equilibrium temperature of dust particles with a 1 μm radius and an albedo of zero as a function of the distance from the star in units of planet e's semimajor axis. Planet e's semimajor axis (0.015 AU) is at a point, where dust particles live for several days, but only a little closer to the star, they evaporate fast.

particles as a function of their radius. It is clearly visible that the temperature is constant for larger particles but starts to increase with a radius smaller than 0.5 μm. This comes from the fact that the cross-sections decrease faster for longer wavelengths (Fig. 3.4a). The Planck function of the star has a larger contribution on the shorter wavelengths than the dust particles. The integral over the Planck function times the cross-sections decreases therefore slower than that of the dust particles. The contribution of the mass loss rate in the energy balance in Equation 2.23 is neglectable. The only way to balance the faster decrease of the integral over the Planck function and cross-sections of the dust is therefore to increase the temperature and thereby the dust particle's Planck function.

The lifetime is very short for small particles because they are warmer and less mass has to sublimate for the particle to disappear. The lifetime increases for particles larger than 0.4 μm. The temperature is almost constant at that point and the particle size determines the lifetime.

Another thing that influences the lifetime of the particle is the distance from the star. I simulated the lifetime of a 1 μm sized particle at different distances from the star, shown in Fig. 4.3b. Planet e's semimajor axis (0.015 AU) is at a point where the particles can live for several days but sublimate fast if they are a bit closer to the star. This means that a dust cloud, which could surround planet e, could not have a large extent inwards. The reason the shape of the temperature curve is different between Fig. 4.3b and Fig. 4.3a is that the temperature in Fig. 4.3b is the equilibrium temperature (for an albedo of zero).

Grain size	0.1 μm	0.2 μm	0.3 μm	0.4 μm	0.5 μm	0.6 μm	0.7 μm
My simulation	7.2 s	216 s	1,512 s	25,275 s	130,477 s	337,426 s	615,230 s
Reference	4.43 s	422 s	5,887 s	25,859 s	65,889 s	113,997 s	168,263 s

Table 4.1: The lifetime of dust according to my simulation and by Valdés et al. [2023] are shown in the table.

Let us now compare those results to those by Valdés et al. [2023], who simulated carbon dust particles around 55 Cnc e with the same parameters that I used but got significantly different results. There are a few differences in the method between my model and theirs. They simulated particles with a radius between 0.1 and 0.7 μm using the same equations for the mass-loss rate, temperature, and beta-factor as I did. They also used LX-MIE to calculate the cross-sections and the asymmetry parameters. They pre-tabulated the cross-sections and the asymmetry parameters as well as the "equilibrium temperature" for each grain size, but they did not interpolate between the values and did not state the step size of their grid. It is not clear what they mean by "equilibrium temperature", because the temperature their equation gives, depends on the decay of the particle, which immediately changes the size and thereby the cross-sections and the asymmetry parameters as well as the surface area, which changes the temperature. Those decaying particles are not in a state of one equilibrium temperature, because it constantly changes. The temperature depends strongly on the distance from the star, which is explicitly in the equation, as discussed above. It was not mentioned that the pre-tabulated temperatures take that into account. If we assume the particles to be at a constant distance equal to the semi-major axis of planet e, we can compare the lifetimes from Valdés et al. [2023] to those in Fig. 4.3a.

The lifetimes of my simulations and by Valdés et al. [2023] are shown in Table 4.1. My results for the lifetime of particles with radii of 0.4 and 0.1 μm are approximately the same as the results by Valdés et al. [2023]. For particles with radii of 0.2 and 0.3 μm, their particles live longer. Starting from 0.5 μm the particles in my simulations live much longer. This might be an inaccuracy on their side from the pre-tabulation of the temperature or from not interpolating between the cross-sections. Another difference might be the chosen distance between the particles and the star. Another possibility is that the simulation might be done for particles that are not stationary. To check this possibility, I simulated 1000 particles with an initial radius of 0.7 μm moving in the system which resulted in a lifetime of 241908 s. This value is closer to the value found by Valdés et al. [2023], but it cannot be determined by it whether the pre-tabulated temperature was a function of distance and simulated moving particles or if the temperature was pre-tabulated for a smaller fixed distance. We obtain qualitatively different lifetimes and with the limited information provided in Valdés et al. [2023] it is not possible to determine what is the difference in methodology. Nevertheless, our work agrees with theirs in that dust may survive for several orbits of planet e.

After looking at the behaviour of stationary dust particles, let us now look at their move-

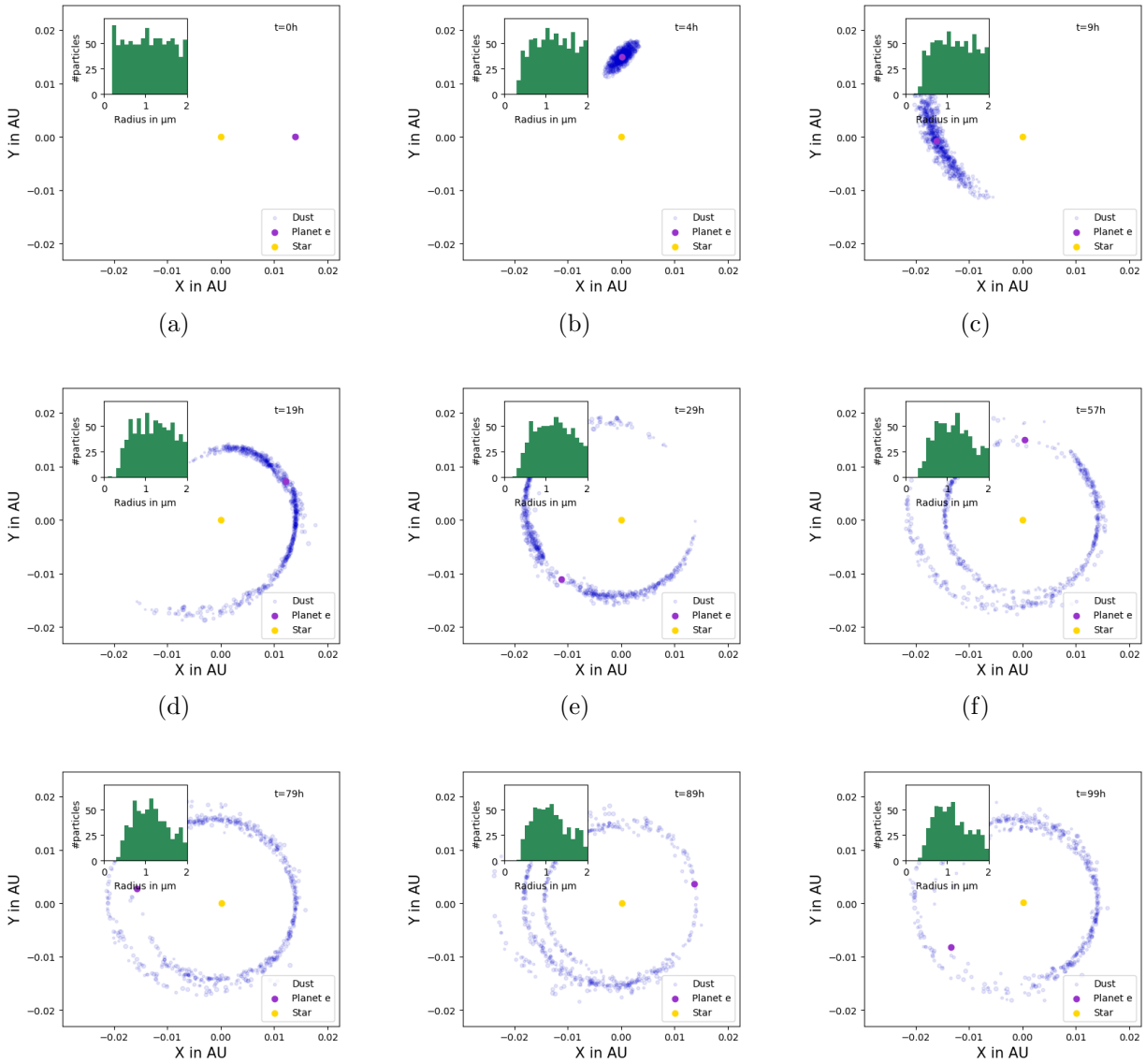

Figure 4.4: The figure shows the behaviour of dust particles emitted into random directions at a speed between 1 and 1.5 times the escape velocity. The initial radius of the particles is randomly taken from a uniform distribution between 0.1 and 2 μm The inset shows the distribution of particle sizes at the moment of each figure. The simulation was done with all planets, but this plot is zoomed in on planet e and the dust to make its behaviour better visible. In the upper right corner is the time that has passed since the particles were ejected.

ment. Fig. 4.4 shows the position of dust particles, planet e and the star at different times. 1000 dust particles are emitted at $t = 0$ in random directions with a velocity randomly chosen between 1 and 1.5 times the escape velocity, pointing into a random direction away from the planet (as described in Section 3.3). The particles are emitted at the surface of the planet. The initial radii are uniformly distributed between 0.1 and 2 μm because they are probably emitted by volcanos (see Section 2.5.1). In the plots, the larger particles are represented by larger dots. The particles form a cloud around the planet, and over two orbits (one orbit takes 17,7 h) the particles have formed a ring around the star. The particles that come closer to the star sublimate, the ones as far away as planet e or farther continue to form rings. The particles drift away from the star due to the radiation pressure. They form a spiral, which is visible in Fig. 4.4f, 4.4g and 4.4h and to some extend also in Fig. 4.4i.

In the upper left corner of the plots in Fig. 4.4 there is the distribution of the dust particle's radii. In the beginning, they were almost equally distributed, because they were randomly chosen from a uniform distribution. The particles smaller than 0.5 μm decay very fast, as would be expected from Fig. 4.3a. There are always some particles with this size because larger particles keep decaying. Starting from Fig. 4.4e most of the particles have a radius around 1 μm as would be expected, because the larger particles decay and become this size.

This means that the dust particles start to form a ring after 20 to 30 hours, which slightly changes its shape but survives longer than one hundred hours, which are about 5.5 orbits of planet e. There is nothing distinct about the time of the secondary eclipse, which could explain the observed change in occultation depth. The very first secondary eclipse could have an unexpected signal because the cloud could still be visible on both sides of the star and reflect light, which would make the occultation depth less deep than it would be without the dust. But this effect would cease to exist as soon as the dust is uniformly distributed around the star. The observed variations in occultation depth are therefore probably not created by dust as the dust is quickly distributed around the entire orbit of the planet.

4.3 Pulsar timing varitaions

To decide, if the gravity of a moon would be large enough to create a measurable signal, I will first look at simulations of the system with a moon and compare them to the simulation without the moon. I will then discuss other sources that could be responsible for a change in the pulse arriving timing and see, how they can be distinguished from the signal of a moon.

Adding a moon to the planetary system around PSR 1257+12 results in a change in the pulse arriving. This change is expected to have the periodicity of the orbiting time of the moon. I used the parameters listed in Tabel 3.3 for the simulation. I will in all plots in this subsection plot only the difference between the signal of the simulation with the moon

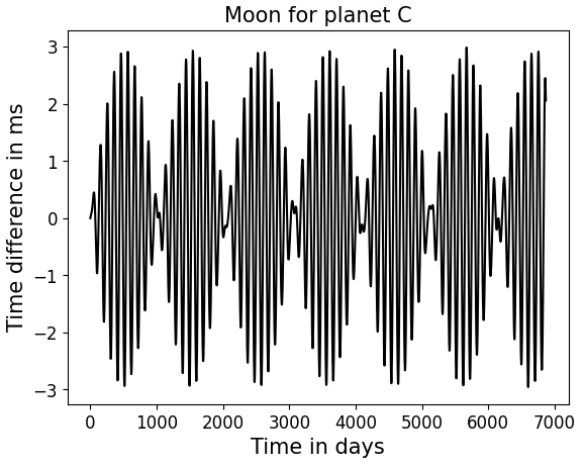

(a) Pulse timing due to planet C with a moon at a distance of 10^5 km

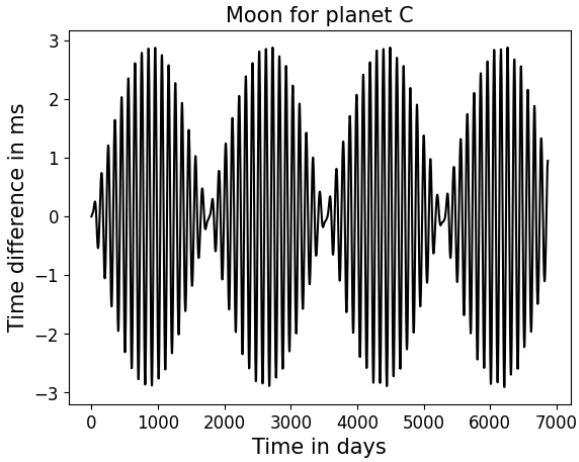

(b) Pulse timing due to planet C with a moon at a distance of $3 \cdot 10^5$ km

Figure 4.5: The plots show the change in pulse arrival time occasioned by a moon of one Earth-mass around planet C over time for different orbital distances. The different orbital distances change the orbiting times (for Fig. 4.5a it is 2.14 days and for Fig. 4.5b it is 11.11 days) and thereby the amplitude modulation of the signal.

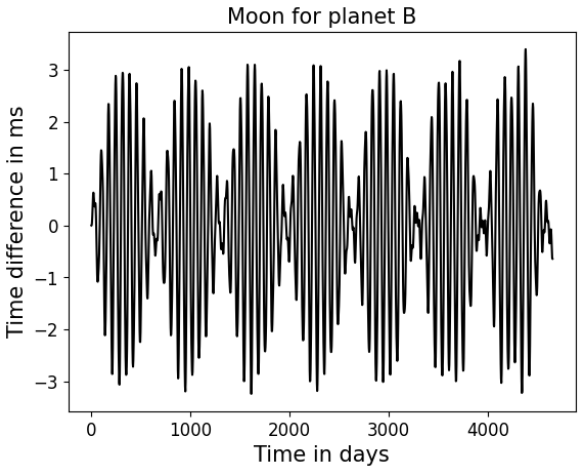

(a) Pulse timing due to planet B with a moon at a distance of 10^5 km

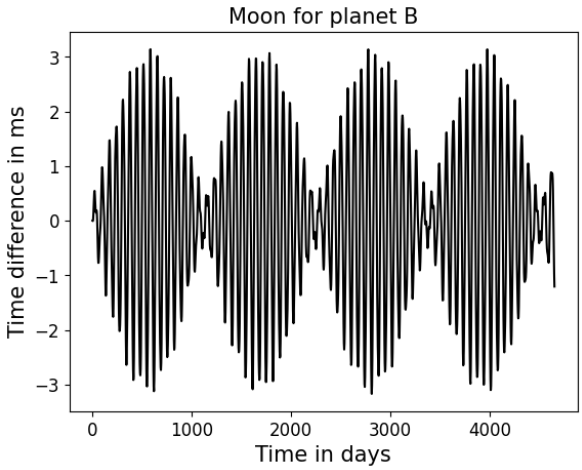

(b) Pulse timing due to planet B with a moon at a distance of $3 \cdot 10^5$ km

Figure 4.6: The plots show the change in pulse arrival time occasioned by a moon of one Earth-mass around planet C over time for different orbital distances. It is the same plot as Fig. 4.5 but for planet B instead of planet C. The different orbital distances change the orbiting times (for Fig. 4.5a it is 2.01 days and for Fig. 4.5b it is 10.12 days) and thereby the amplitude modulation of the signal.

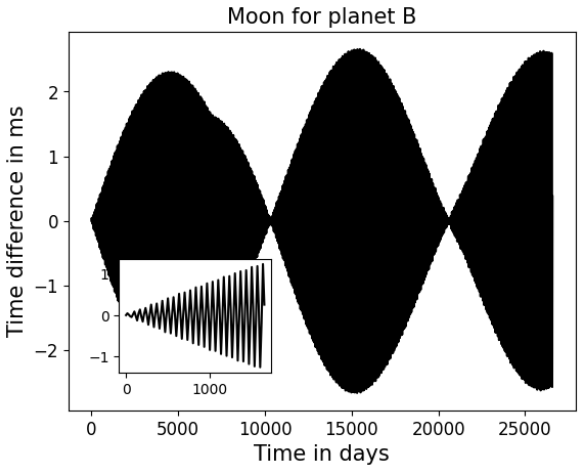

(a) Pulse timing due to planet B with a moon ($0.1\,M_\oplus$)

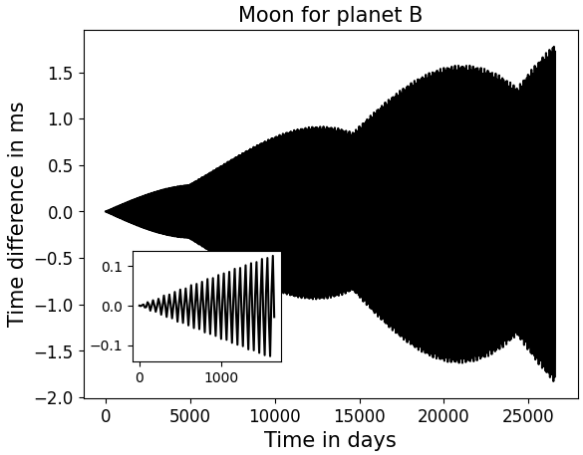

(b) Pulse timing due to planet B with a moon ($0.01\,M_\oplus$)

Figure 4.7: The plots show the change in pulse arrival time from a moon of $0.1\,M_\oplus$ (Fig. 4.7a) and $0.01\,M_\oplus$ (Fig. 4.7b) around planet B over time at a distance of $3 \cdot 10^5$ km (this is equivalent to an orbiting time of 9.14 days for Fig. 4.7a and 9.24 days for Fig. 4.7b).

subtracted from the signal of the simulation without the moon as discussed in Section 3.4. I varied the moon's mass and the distance between the moon and the planet. All parameters I used are listed in Table 3.4.

In Fig. 4.5b it is visible that the amplitude in the pulse timing does not grow infinitely. It is an amplitude modulation, but the amplitude cannot become larger than 3 ms, because the combined gravity of the three planets cannot make an arbitrarily large displacement in the position of the pulsar, with the combined gravitation of the mass of all the planets together. Comparing this to Fig. 4.10a, which is the same configuration, but with a distance between the moon and planet of 10^5 km instead of $3 \cdot 10^5$ km it is visible that the change in the orbiting period of the moon (the consequence of the change of distance) changes the periodicity of the amplitude modulation. Fig. 4.6 shows the same two situations but this time the moon is around planet B instead of planet C. The pattern is the same, the moon with the shorter orbiting time has a shorter change in its amplitude modulation than the other. But comparing the timescales of Fig. 4.5 and Fig. 4.6 it is visible that the orbital period of the host planet plays an important role. Both cases have been simulated for 70 orbital periods of the respective host planet and the pattern, the number of maxima in the amplitude modulation is nearly the same. The small differences between the number of amplitude modulation periods could come from the fact that the moon's orbital period is different between the planets due to the different masses of the planets (and the same distance between the planet and the moon).

So far I only compared moons of the same mass but at different distances. Let us now look at the effect of a change in the mass of the moon. By changing the mass I also changed the

orbiting period a bit, because I was subtracting a different amount of mass from the planet, but this change is small, as can be seen in Table 3.4. In Fig. 4.7 the moons of planet B are at a distance of $3 \cdot 10^5$ km so at the same distance as in Fig. 4.6b but this time instead of having a mass of $1\,M_\oplus$ they have $0.1\,M_\oplus$ (Fig. 4.7a) and $0.01\,M_\oplus$ (Fig. 4.7b). The period of the amplitude variation gets longer with a decrease in the mass of the moon (notice the difference in the time scale between Fig. 4.6b and Fig. 4.7). This change cannot come completely from the change in the orbiting period of the moon, because the difference in the orbiting period between Fig. 4.6a and Fig. 4.6b is much larger than that between Fig. 4.6b and Fig. 4.7a or Fig. 4.7b. This change comes probably from the fact that the smaller masses of the moons make the effect the moons have on the system smaller. This means that it takes a longer time until they have changed it up completely (this is the maximum in the amplitude modulation) and also longer until the system happens to intersect with its "normal" state again.

It is visible in the plots that the shape of the amplitude modulation changes with the mass of the moons. For a moon with a mass of $0.1\,M_\oplus$ this change is not big, it is only visible in the shape of the first peak (see Fig. 4.7a), but the shape of the amplitude modulation in the case of a mass of $0.1\,M_\oplus$ is very different (see Fig. 4.7b). If a moon should be measured, its mass could therefore be determined by inferring the periodicity of its amplitude variation difference from the measured signal. The maximal amplitude is not a meaningful parameter, since it seems to be the same for all moon masses. How small a moon can be in order to still be detectable therefore does not so much depend on the accuracy of the measurement but on the accuracy of a model over longer times (which includes a need to have accuracy on the planet masses) or of analysing the data.

It is remarkable that there is such a periodicity in the difference between the signal with and without the moon. This is not expected since the systems are both chaotic since they are both many-body systems. One thing that could prevent the difference between those systems from becoming chaotic is the resonance between the planetary orbits. Planet B and C are close to a 2:3 resonance and planet A and C are close to a 1:4 resonance. To see if the effect of the resonances between the planets are the reason for the periodicity, I made a simulation where I changed the orbiting period of planet C to 110 days. This corresponds to a distance from the pulsar of 0.5 AU. I made a simulation with the new system with only the three planets and one where planet B has a moon of 1 Earth mass at a distance of $3 \cdot 10^5$ km. The result is shown in Fig. 4.8a, Fig. 4.8b shows the same but this time with the normal distance for planet C. It is clearly visible that the change in distance and orbiting period for planet C does not have a great influence on the signal. The hyper-period seems therefore not to come from the resonance between the planetary orbits.

To check, if there is a problem with the simulations, I compared the initial position of the planet without the moon (R_P) and the position of the barycentre in the case with the moon (R_M) to each other. There is a difference between them, for a moon of one Earth mass it is $\frac{R_P}{R_M} = 0.9999426$, for a mass of $0.1 M_\oplus$ it is $\frac{R_P}{R_M} = 0.9999943$ and for a mass

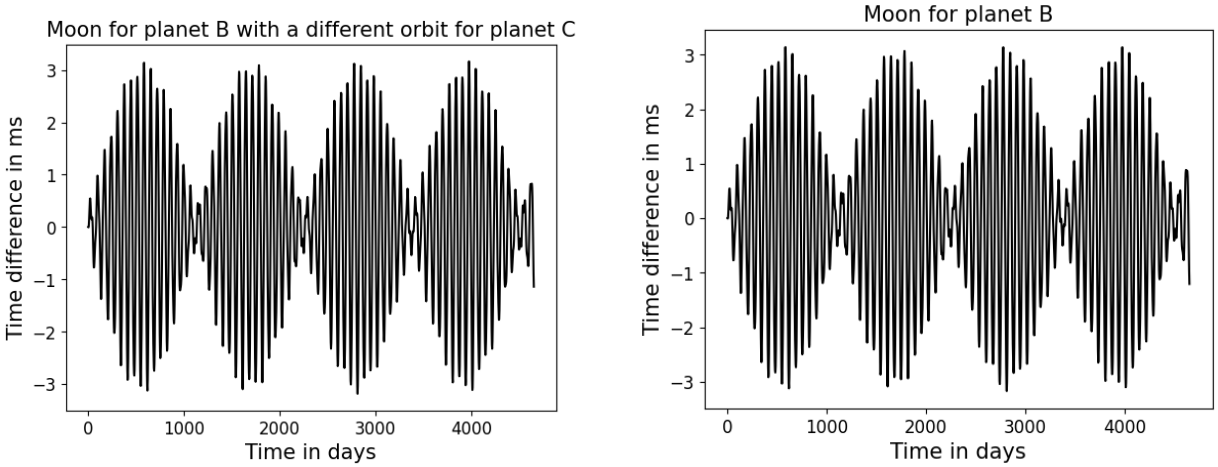

(a) Pulse timing variation with a broken orbital resonance

(b) Pulse timing variation without a broken orbital resonance

Figure 4.8: The figures show the difference in the pulse timing variation over time. Fig. 4.8b shows the difference between the normal system with three planets and the one with a moon around planet B of the mass of the Earth at a distance of $3 \cdot 10^5$ km. It is the same as in Fig. 4.6b and shown here again for comparison. Fig. 4.8a shows the same but this time the orbital period of planet C is 110 days, which interrupts the resonance between the orbits of the planets.

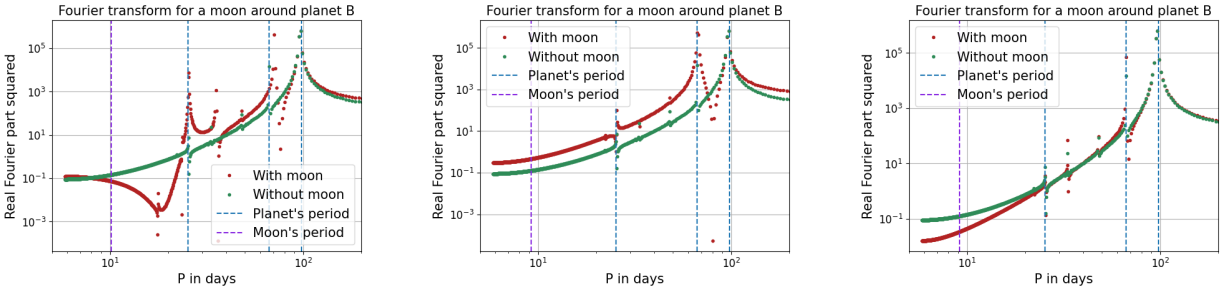

(a) Moon of 1 Earth mass (b) Moon of 0.1 Earth mass (c) Moon of 0.01 Earth mass

Figure 4.9: The plots show the squared real part of the Fourier transform of the change in the pulse arriving time for different periods (the inverse frequencies). The green dots are the simulation with only the three planets, it is therefore the same in all three plots. The red dots are from the simulation with a moon around planet B with different masses. The three blue lines mark the orbital period of the three planets and the purple line is the orbital period of the moon. This changes slightly for each of the masses.

of $0.01 M_\oplus$ it is $\frac{R_P}{R_M} = 0.9999994$. This could accelerate the divergence between the two systems. The faster divergence for the system with the larger moon would be consistent with this explanation, but I did not have time to investigate this further.

Another way of analysing what could cause the periodicity is looking at the Fourier-transformed signal. Fig. 4.9 shows the Fourier transformed signals of the system with and without a moon around planet B as well as lines that indicate the orbital periods of the planets and moon. There is no peak at the orbital period of the moon for any of the three moon masses. This is not surprising, because the moon does not directly affect the movement of the pulsar. The pulsar gets in a good estimation pulled by the planet-moon system towards their centre of mass and this does not change by the orbiting period of the moon. The effect the moon has to come from its interaction with the other planets. The way they interact with the planet in close encounters changes with the presence of a moon. These disturbances in the orbits of the other planets will then have an influence on the pulsar's motion. It makes therefore sense that the Fourier transform on the periodicity of planet A should increase with an increase in the mass of the moon. It is the lightest planet ($0.02 M_\oplus$) and therefore also the one which can be most easily disturbed and this disturbance of course increases with an increase in the moon's mass.

Let us now discuss other sources that could change the pulse arrival time. The first question to answer is if this pulse arrival timing can be distinguished from that of an additional planet with the same orbiting period. I chose the parameters of the moon as listed in the last row of Table 3.4 and made the planet in the other simulation with the same mass and orbiting period (which is equivalent to a distance between planet and pulsar of $1.64 \cdot 10^8$ km). The results of the simulations are shown in Fig. 4.10. It is evident that the shape of the change in the pulse arrival timing is very different and therefore easy to

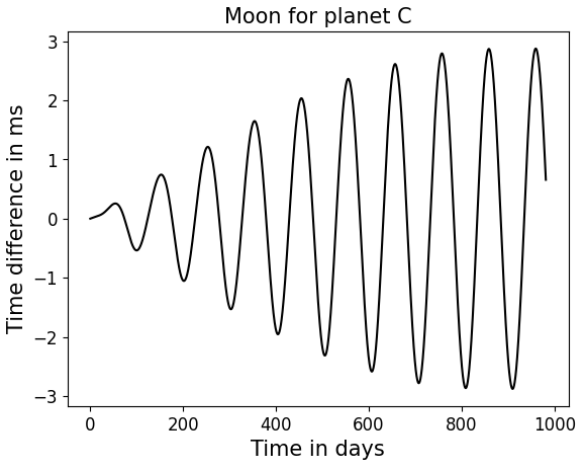

(a) Pulse timing planet C with moon

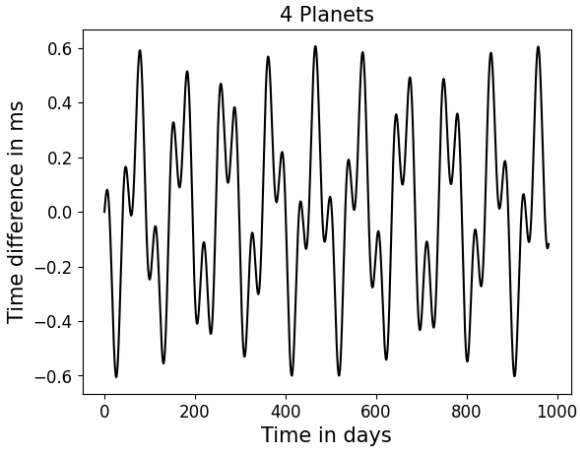

(b) Pulse timing four planets

Figure 4.10: The plots show the change in the pulse arrival time over time. Fig. 4.10a shows the difference between planet C with a moon with the parameters as listed in the bottom row of Table 3.4 and the system with only the three planets. Fig. 4.10b shows the difference between the system with an added planet, which has the same orbital period and mass as the moon in Fig. 4.10a and the system with only the three planets.

distinguish. The line shape in Fig. 4.10b is very different from any of the other plots. This comes from the fact that, in order not to add any mass to the system, I subtracted the mass of the fourth planet from the mass of planet C. This makes it moreover better comparable to the simulation in Fig. 4.10a, where I did the same. If I do not subtract the mass of the fourth planet from planet C, I get a sin-wave as a result, which does not change its amplitude even over longer times (Fig. 4.11).

Another thing to consider is the uncertainty of the planets' masses of about 5%. A change in mass would change the movement of the pulsar, so I simulated the system with the assumed masses and the mass of a planet increased or decreased by 5% for planet B (Fig. 4.12) and planet C (Fig. 4.13). The effect is similar in both cases, the amplitude is much smaller than that of a moon and the amplitude variation is so small that it can easily be distinguished from the signal of a moon.

5 Conclusion

After describing the results in some detail, let us now summarize the most important points: I have done simulations on the TTVs of 55 Cnc e to find the influence the inclination of the orbits of the other planets in the system has on them. The result is that the orbits would have to be at nearly a right angle to have a measurable effect on planet e's TTVs.

Dust particles, launched by volcanic activity on 55 Cnc e can live long enough to form a

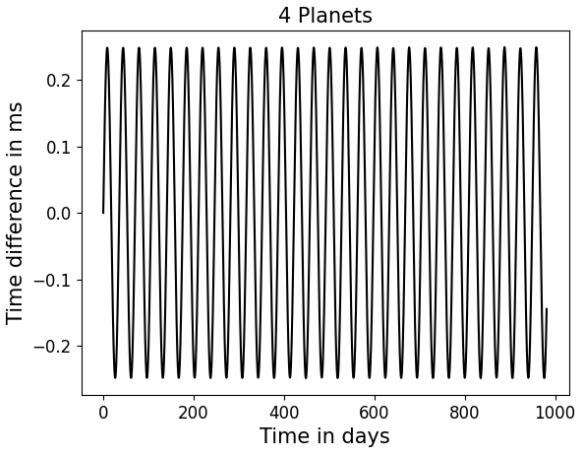

(a) Pulse timing four planet

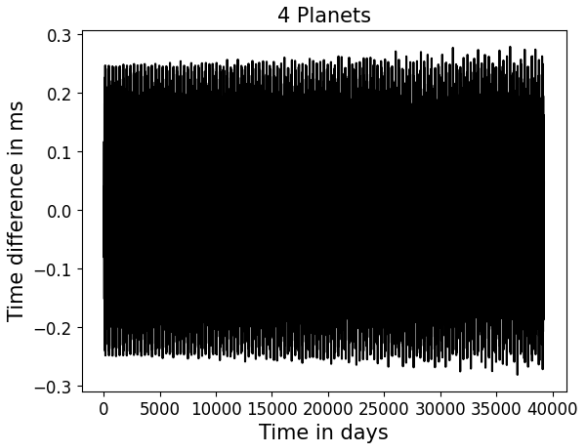

(b) Pulse timing four planets over a long time period

Figure 4.11: The figure shows the change in the pulse arrival time over time for adding another planet with the mass of the Earth (without subtracting the mass from one of the other planets) and an orbiting period of 11.11 days to the system.

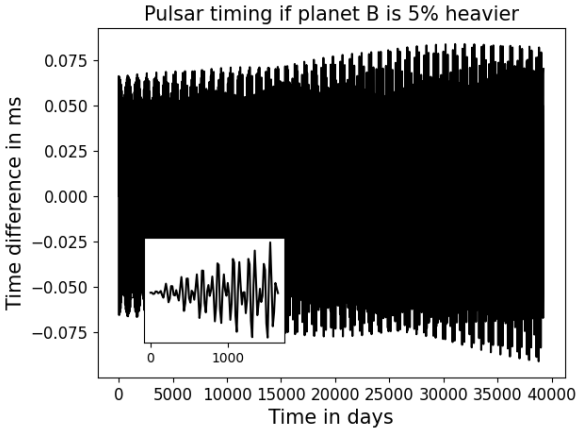

(a) Pulse timing variation planet B heavier

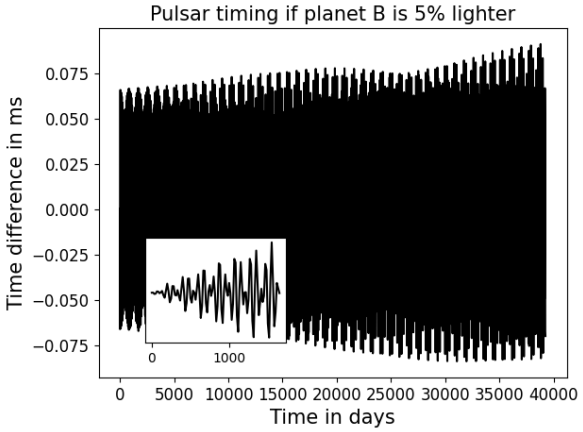

(b) Pulse timing variation planet B lighter

Figure 4.12: The plot shows the difference in the pulse arriving timing between a simulation with the masses as they are assumed to be and the same simulation but with planet B 5% heavier or lighter respectively.

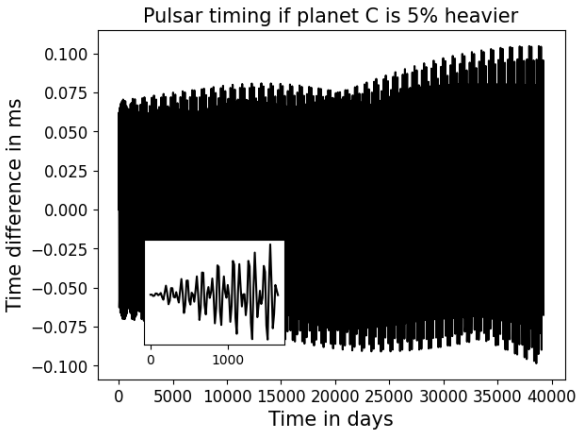

(a) Pulse timing variation planet C heavier

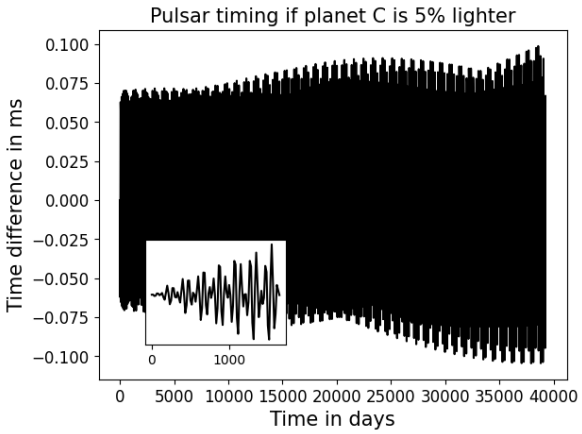

(b) Pulse timing variation planet C lighter

Figure 4.13: The plot shows the difference in the pulse arriving timing between a simulation with the masses as they are assumed to be and the same simulation but with planet C 5% heavier or lighter respectively.

cloud around the planet if they do not come too close to the star. But they distribute themselves at a ring around the star at the distance from it of planet e's semi-major axis, which makes it unlikely that this dust should cause the observed irregularity in the occultation depth.

I also simulated the effect a moon around one of the planets of the pulsar PSR B1257+12 would have on the movement of this pulsar. The effect is a measurable signal with a hyperperiod for which I could not find the exact source. The signal of a moon is different from the signal other sources could produce, such as a fourth planet or the uncertainty of the known planets' masses. This means that a moon may be detectable and identifiable if observations are sustained for a sufficiently long amount of time.

A Transit timing variations

This is the code I used for the transit timing variations:

```
import rebound
from astropy import constants as const
import numpy as np
from joblib import Parallel, delayed

#Define some constants:
M_J = const.M_jup.value / (const.M_sun.value * 0.92)
```

```
M_E = const.M_earth.value / (const.M_sun.value * 0.92)


def inclination(k, j):
    #Set up the simulation with the stars and planets. The inclinaion and longitude of the acending node are the variables k and j:
    sim=None
    sim=rebound.Simulation()
    sim.add(m=1)
    sim.add(m=7.99 * M_E, a=1, e=0.028)
    sim.add(m=0.84 * M_J / np.abs(np.cos(k)), a = 0.11 / 0.015, e = 0.0023, inc = k, Omega = j)
    sim.add(m=0.178 * M_J / np.abs(np.cos(k)), a = 0.237 / 0.015, e = 0.072, inc = k, Omega = j)
    sim.add(m=0.148 * M_J / np.abs(np.cos(k)), a = 0.773 / 0.015, e = 0.08, inc = k, Omega = j)
    sim.add(m=3.84 * M_J / np.abs(np.cos(k)), a = 5.4 / 0.015, e = 0.027, inc = k, Omega = j)
    sim.add(m=0.264 * 0.92 / np.abs(np.cos(k)), a = 1050 / 0.015, inc = k, Omega = j)

    ###########################################################

    N=5000 #Number of transits

    #Set up arrays to save the results in:
    transittimes = np.zeros(N)
    position = np.zeros((N,6))

    p = sim.particles
    i = 0 #counds the number of transits already simulated

    period = 0.7365474 #orbital period o fplanet e in days

    while i < N:
        distance_old = ((p[1].y - p[0].y)**2 + (p[1].z - p[0].z)**2)**0.5 + 5 #Set up the variable "distance_old" with a large value

        while ((p[1].y - p[0].y)**2 + (p[1].z - p[0].z)**2)**0.5 < distance_old:  #This condition is true as long as the distance between star and planet becomes smaller with every step
            distance_old = ((p[1].y - p[0].y)**2 + (p[1].z - p[0].z)**2)**0.5 #Update the variable "distance_old"
```

```
            sim.integrate(sim.t + 2 * np.pi / (period * 24 * 3600 * 10))
            ↪  #Integrate for 0.1 seconds

        transittimes[i] = sim.t #Save the time of the transit
        position[i,3:] = np.array([p[1].x - p[0].x, p[1].y - p[0].y, p[1].z
        ↪  - p[0].z]) #Save the position of planet e at the transit
        sim.integrate(sim.t + 2 * np.pi * 0.99) #Integrate over 99\% of the
        ↪  orbit
        i += 1
    #Save the results:
    np.savetxt(f"Inc_{k}_long{j}_N_{N}_transit_center_mass.txt",
    ↪  transittimes, delimiter =", ")
    np.savetxt(f"Inc_{k}_long{j}_N_{N}_position_transit_center_mass.txt",
    ↪  position, delimiter =" ")
    return 0

ks = np.arange(0.6,2,0.02)
js = np.arange(0,3.2,0.1)

#Run the simulations in parallel:
res = Parallel(n_jobs=5)(delayed(inclination)(k, j) for k in ks for j in
↪  js)
```

B Dust particles

This is the code I used to simulate the dust particles:

```
import reboundx
import rebound
from astropy import constants as const
import numpy as np
import time
from scipy.optimize import fsolve
import os
from joblib import Parallel, delayed


#Define some constants:
M_J = const.M_jup.value / (const.M_sun.value * 0.92)
M_E = const.M_earth.value / (const.M_sun.value * 0.92)
R_E = const.R_earth.value / (0.015 * const.au.value)
R_S = const.R_sun.value / (0.015 * const.au.value)
```

```
period = 0.7365474    #orbital period in days



Escape_velocity = (2 * 7.99 * M_E / (1.853 * R_E)) ** 0.5


Integration_time = 3600 * 100 #Total time of integration in seconds
tot_int_time = Integration_time * (2 * np.pi) / (period * 24 * 3600)  #Transforming the seconds into rad
dust_time = 1     #Number of times the dust gets emitted to the system
Number_points = 10000   #Must be a multiple of dust_times
N_dust = 1    #Number of dust praticles emitted each time
d = 1.853 * R_E      #Distance from the center of the planet at wihch the particles are placed from the center of the planet in m
simulations = 1000  #The dust particles do not interact, so instead of one simulation with many particles, I can do many simulations with one particle. This has the advantage that they can run in parallel.


#efficiency constant has the units g/(s*(\mu m)^2):
#Carbon
mu = 12  #molecular weight
H = 64825257 * 10 ** (4)  #Latend heat
P_0 = np.exp(36.7)  #sublimation pressure
Density = 2.16
A = 93646  #mu * m_mu * H / k_B

k_B = 1.380649*10**(-16)  #Boltzmann-constant in cm^2 g/(s^2 K)
m_mu = 1.66053906660*10**(-24)  #atomic mass unit in g
c = 2.99792458e10 #speed of light in cm/s
h = 6.62607015e-27 #Planck constant in erg s
R_star = 0.943*const.R_sun.value*100      #in cm
M_star = const.M_sun.value * 0.92 * 1000  #in g
r_star_dust = 0.015 * const.au.value*100     #in cm
T_star = 5234   #in K
G = 6.67430 * 10**(-8) #gravitational constant in dyn cm^2/g^2
```

```
def dust_simulation (simulation_index):
    #Set up the simulation with all the planets and the stars:
    sim = None
    sim = rebound.Simulation()
    sim.add(m = 1, r = 0.943 * R_S)
    sim.add(m = 7.99 * M_E, a = 1, e  = 0.07, r = 1.853 * R_E)
    sim.add(m = 0.89 * M_J, a = 0.11 / 0.015, e = 0.02)
    sim.add(m = 0.25 * M_J, a = 0.24 / 0.015, e = 0.339)
    sim.add(m = 0.144 * M_J, a = 0.781 / 0.015, e = 0.3)
    sim.add(m = 4.05 * M_J, a = 5.9 / 0.015, e = 0.16)
    sim.add(m = 0.264 * 0.92, a = 1050 / 0.015)

    #Import the radiational force:
    rebx = reboundx.Extras(sim)
    rf = rebx.load_force("radiation_forces")
    rebx.add_force(rf)
    rf.params["c"] = const.c.value / (0.015 * const.au.value) / (2 * np.pi)
    ↪  * (period * 24 * 3600)  #Is the speet of light in the used units
    p = sim.particles

    #The values will be saved in those arrays later:
    position = np.zeros((3, N_dust * dust_time, Number_points))
    planet_e_position = np.zeros((3, Number_points))
    planet_b_position = np.zeros((3, Number_points))
    star_position = np.zeros((3, Number_points))
    velocity = np.zeros((3, N_dust * dust_time, Number_points))
    Particle_radius = np.zeros((N_dust * dust_time, Number_points))
    Particle_temperature = np.zeros((N_dust * dust_time, Number_points))
    Particle_beta = np.zeros((N_dust * dust_time, Number_points))

    #Planck function as a function of the wavelength and the temperature
    def Planck(wl,x):
        factor = 2 * h * c ** 2
        B=(factor / wl ** 5) / (np.exp(h * c / (wl * k_B * x)) - 1)
        return(B)

    Wave_length = np.load('Wavelength.npy') #load the wavelength-grid from
    ↪  LX-MIE
    a=150
    Wave_length = Wave_length[a:]#The cross-sections for the shortest
    ↪  wavelengths are so small that they can be neglected, these
    ↪  wavelength don't have to be considered

```

```
    #This is the energy-balance that needs to be solved in order to get the
    ↪  temperature:
    def func(x):
        alpha_x = (mu * m_mu / (2 * np.pi * k_B * x))**0.5 * P_0 *
        ↪  np.exp(-A/x)
        dmdt_x = 4 * np.pi * (R_dust * 10 ** (-4)) ** 2 * alpha_x
        Integral_dust = cross_section[a:] *  Planck(Wave_length,x)
        Integral_star = cross_section[a:] * Planck(Wave_length,T_star)
        Omega = 2 * np.pi * (1 - (1 - (R_star / r_star_dust) ** 2) ** 0.5)

        Integrated_star = np.trapz(Integral_star,Wave_length)
        Integrated_dust = np.trapz(Integral_dust,Wave_length)

        return(Omega * Integrated_star - 4 * np.pi * Integrated_dust) -
        ↪  dmdt_x * H

    #This function loads the cross-sections:
    def func_cross_sections(x, name):
        if 0.001 <= x < 0.1:
            array_R_dust = np.arange(0.001, 0.1, 0.001)
            collected_cross_section =
            ↪  np.load(f'{name}_0.001_0.1_0.001.npy')
        if 0.1 <= x < 10:
            array_R_dust = np.arange(0.1, 10, 0.001)
            collected_cross_section = np.load(f'{name}_0.1_10_0.001.npy')
        if 10 <= x < 50:
            array_R_dust = np.arange(10, 50, 0.1)
            collected_cross_section = np.load(f'{name}_10_50_0.1.npy')
        if 50 <= x < 200:
            array_R_dust = np.arange(50, 200, 0.1)
            collected_cross_section = np.load(f'{name}_50_200_0.1.npy')
        if 200 <= x < 400:
            array_R_dust = np.arange(200, 400, 0.1)
            collected_cross_section = np.load(f'{name}_200_400_0.1.npy')
        if 400 <= x < 700:
            array_R_dust = np.arange(400, 700, 0.1)
            collected_cross_section = np.load(f'{name}_400_700_0.1.npy')
        if 700 <= x < 1000:
            array_R_dust = np.arange(700, 1000, 0.1)
            collected_cross_section = np.load(f'{name}_700_1000_0.1.npy')
        if 1000 <= x < 1300:
            array_R_dust = np.arange(1000, 1300, 0.1)
            collected_cross_section = np.load(f'{name}_1000_1300_0.1.npy')
        if 1300 <= x < 1500:
```

```
            array_R_dust = np.arange(1300, 1500, 0.1)
            collected_cross_section = np.load(f'{name}_1300_1500_0.1.npy')
        if x == 1500 or x > 1500:
            array_R_dust = np.arange(1500, 1500.1, 0.1)
            collected_cross_section =
            ↪  np.load(f'{name}_1500_1500.1_0.1.npy')
        return array_R_dust, collected_cross_section

    #This function does the interpolation between the cross-sections:
    def func_interpolate(x, name):
        array_R_dust, collected_cross_section = func_cross_sections(x,
        ↪  name)
        index_radius = np.argmin(np.abs(x-array_R_dust))

        if array_R_dust[index_radius] == x:
            cross_section = collected_cross_section[index_radius,:]

        if index_radius == len(array_R_dust) - 1 and
        ↪  array_R_dust[index_radius] < x and index_radius != 0:
            array_R_dust_2, collected_cross_section_2 =
            ↪  func_cross_sections(x + 0.1, name)
            index_radius_2 = np.argmin(np.abs(x-array_R_dust_2))
            R_1 = array_R_dust[index_radius]
            R_2 = array_R_dust_2[index_radius_2]
            cross_section_1 = collected_cross_section[index_radius,:]
            cross_section_2 = collected_cross_section_2[index_radius_2,:]
            cross_section = (x - R_1) / (R_2 - R_1) * (cross_section_2 -
            ↪  cross_section_1) + cross_section_1

        if array_R_dust[index_radius] < x and index_radius !=
        ↪  len(array_R_dust) -1:
            R_1 = array_R_dust[index_radius]
            R_2 = array_R_dust[index_radius + 1]
            cross_section_1 = collected_cross_section[index_radius,:]
            cross_section_2 = collected_cross_section[index_radius + 1,:]
            cross_section = (x - R_1) / (R_2 - R_1) * (cross_section_2 -
            ↪  cross_section_1) + cross_section_1

        if index_radius == 0 and array_R_dust[index_radius] > x:
            array_R_dust_1, collected_cross_section_1 =
            ↪  func_cross_sections(x - 0.1, name)
            index_radius_1 = np.argmin(np.abs(R_dust-array_R_dust_1))
            R_1 = array_R_dust_1[index_radius_1]
            R_2 = array_R_dust[index_radius]
```

```
            cross_section_1 = collected_cross_section_1[index_radius_1,:]
            cross_section_2 = collected_cross_section[index_radius,:]
            cross_section = (x - R_1) / (R_2 - R_1) * (cross_section_2 -
            ↪  cross_section_1) + cross_section_1

        if array_R_dust[index_radius] > x and index_radius != 0:
            R_1 = array_R_dust[index_radius - 1]
            R_2 = array_R_dust[index_radius]
            cross_section_1 = collected_cross_section[index_radius - 1,:]
            cross_section_2 = collected_cross_section[index_radius,:]
            cross_section = (x - R_1) / (R_2 - R_1) * (cross_section_2 -
            ↪  cross_section_1) + cross_section_1
        return cross_section

    Removed_particles = 0 #Number of dust particles that have been removed
    ↪  from the system
    T = 2360  #Initial guess for the temperature of the dust in K

    for i in range(dust_time):
        #Loop to add all the particles:
        for j in range(i * N_dust + 7 - Removed_particles,
                       i * N_dust + 7 + N_dust - Removed_particles):

            t_random=int((time.time() - 10 ** 9 * 1.699) * 100)
            np.random.seed(t_random)

            #Randomly chosing a position on the surface of the planet to
            ↪  emit the dust particle:
            theta = np.random.uniform(0, np.pi)
            phi = np.random.uniform(0, 2 * np.pi)
            x_coor = d * np.sin(theta) * np.cos(phi)
            y_coor = d * np.sin(theta) * np.sin(phi)
            z_coor = d * np.cos(theta)

            #Randomly chosing a direction of the particles velocity in the
            ↪  semi-circle pointing away from the planet:
            v_theta = np.random.uniform(-np.pi / 2, np.pi / 2)
            v_phi = np.random.uniform(-np.pi / 2, np.pi / 2)
            v_value = np.random.uniform(1, 1.5)
            v_x = Escape_velocity * v_value * np.sin(theta + v_theta) *
            ↪  np.cos(phi + v_phi)
            v_y = Escape_velocity * v_value * np.sin(theta + v_theta) *
            ↪  np.sin(phi + v_phi)
            v_z = Escape_velocity * v_value * np.cos(theta + v_theta)
```

```
208
209             grain_size = np.random.uniform(0.1, 2)   #Starting grain size
                ↪  in mikro meters
210
211             sim.add(m = 0, x = p[1].x + x_coor, y = p[1].y + y_coor, z =
                ↪  p[1].z + z_coor,
212                     vx = p[1].vx + v_x, vy = p[1].vy + v_y, vz = p[1].vz +
                        ↪  v_z,
213                     r = (grain_size * 10**(-6)) / (0.015 * const.au.value))
                        ↪  #Adding the particle
214
215             #Calculate the beta-factor for the particle:
216             R_dust = grain_size
217             Mass_dust = (4/3 * np.pi * (R_dust * 10**(-4))**3) * Density
218             cross_section = func_interpolate(R_dust, 'cross_sections')
219             cross_section_scatter = func_interpolate(R_dust,
                ↪  'cross_sections_scatter')
220             asymmetry_parameter = func_interpolate(R_dust,
                ↪  'asymmetry_parameter')
221             beta_cross_section = cross_section + (1 - asymmetry_parameter)
                ↪  * cross_section_scatter
222             Integral_for_beta = beta_cross_section[a:] *
                ↪  Planck(Wave_length,T_star)
223             Integrated_beta = np.trapz(Integral_for_beta,Wave_length)
224             beta = np.pi * R_star**2 / (G * M_star * Mass_dust * c) *
                ↪  Integrated_beta  #Ratio of the radiation force to the
                ↪  gravitational force from the star
225             sim.particles[j].beta = beta
226
227
228         integration = np.arange(i * tot_int_time / dust_time, (i + 1) *
            ↪  tot_int_time / dust_time,
229                                 tot_int_time / Number_points)
230
231         for k in range(len(integration)):
232             sim.integrate(integration[k])
233             index = i * Number_points / dust_time + k
234
235             for l in np.linspace(len(p)-1, 7, len(p) - 7):
236                 #Save the position and velocity of the dust particles:
237                 position[:, int(l) - 7, int(index)] =
                    ↪  np.array([p[int(l)].x, p[int(l)].y, p[int(l)].z])
238                 velocity[:, int(l) - 7, int(index)] =
                    ↪  np.array([p[int(l)].vx, p[int(l)].vy, p[int(l)].vz])
```

```
239
240
241                 R_dust = p[int(l)].r * 10**6 * 0.015 * const.au.value
                    ↪  #Radius in \mu m
242                 Particle_radius[int(l) - 7, int(index)] = R_dust #Save
                    ↪  radius of the dust particles
243
244                 r_star_dust = ((p[int(l)].x - p[0].x) ** 2 +  (p[int(l)].y
                    ↪  - p[0].y) ** 2 + (p[int(l)].z - p[0].z) ** 2) ** 0.5 *
                    ↪  0.015 * const.au.value * 100     #distance between star
                    ↪  and dust particle in cm
245
246                 #Calculate the beta-factor:
247                 Mass_dust = (4/3 * np.pi * (R_dust * 10**(-4))**3) *
                    ↪  Density
248                 cross_section = func_interpolate(R_dust, 'cross_sections')
249                 cross_section_scatter = func_interpolate(R_dust,
                    ↪  'cross_sections_scatter')
250                 asymmetry_parameter = func_interpolate(R_dust,
                    ↪  'asymmetry_parameter')
251                 beta_cross_section = cross_section + (1 -
                    ↪  asymmetry_parameter) * cross_section_scatter
252                 Integral_for_beta = beta_cross_section[a:] *
                    ↪  Planck(Wave_length,T_star)
253                 Integrated_beta = np.trapz(Integral_for_beta,Wave_length)
254                 beta = np.pi * R_star**2 / (G * M_star * Mass_dust * c) *
                    ↪  Integrated_beta
255                 Particle_beta[int(l) - 7, int(index)] = beta #Save the
                    ↪  beta-factor
256
257
258                 #Calculate and save the temperature:
259                 T = fsolve(func, T)
260                 Particle_temperature[int(l) - 7, int(index)] = T
261
262
263                 alpha = (mu * m_mu / (2 * np.pi * k_B * T))**0.5 * P_0 *
                    ↪  np.exp(-A/T) #efficiency constant has the units
                    ↪  g/(s*(cm)^2)
264                 d_m = 4 * np.pi * (R_dust * 10**(-4))**2 * alpha *
                    ↪  Integration_time / Number_points #Mass-loss rate in
                    ↪  units of g
265                 M_new = Density * (4/3 * np.pi * (R_dust * 10**(-4))**3) -
                    ↪  d_m #Updated mass
```

```
266
267                 if M_new<0:
268                     sim.remove(int(l))
269                     Removed_particles = Removed_particles + 1
270
271                 else:
272                     R_update = (3/4 * M_new / (Density * np.pi) *
                        ↪  10**12)**(1/3) #Calculate the new radius
273                     if (R_update) < 0.001:
274                         sim.remove(int(l))
275                         Removed_particles = Removed_particles + 1
276                     else:
277                         p[int(l)].r = ((R_update) * 10**(-6)) / (0.015 *
                            ↪  const.au.value) #Save the new radius
278
279             #Save the positions of planets b and e and the star:
280             planet_e_position[:, int(index)] = np.array([p[1].x, p[1].y,
                ↪  p[1].z])
281             planet_b_position[:, int(index)] = np.array([p[2].x, p[2].y,
                ↪  p[2].z])
282             star_position[:, int(index)] = np.array([p[0].x, p[0].y,
                ↪  p[0].z])
283
284     #Save the simulations:
285     np.save(f'position_{simulation_index}.npy',position)
286     np.save(f'planet_e_position_{simulation_index}.npy',planet_e_position)
287     np.save(f'planet_b_position_{simulation_index}.npy',planet_b_position)
288     np.save(f'star_position_{simulation_index}.npy',star_position)
289     np.save(f'velocity_{simulation_index}.npy',velocity)
290     np.save(f'Particle_radius_{simulation_index}.npy',Particle_radius)
291     np.save(f'Particle_temperature_{simulation_index}.npy',
        ↪  Particle_temperature)
292     np.save(f'Particle_beta_{simulation_index}.npy',Particle_beta)
293
294
295 #Run several sinulations in parallel:
296 simulation_numbers = range(simulations)
297 res = Parallel(n_jobs=10)(delayed(dust_simulation)(simulation_index) for
    ↪  simulation_index in simulation_numbers)
298
299 #Set up new arrays to put the different siumulations together:
300 position = np.zeros((3, N_dust * dust_time * simulations, Number_points))
301 velocity = np.zeros((3, N_dust * dust_time * simulations, Number_points))
```

```
Particle_radius = np.zeros((N_dust * dust_time * simulations,
↪  Number_points))
Particle_temperature = np.zeros((N_dust * dust_time * simulations,
↪  Number_points))
Particle_beta = np.zeros((N_dust * dust_time * simulations, Number_points))

#The positions of the planets and the star are the same in all simulations,
↪  so it is enough to load them once:
planet_e_position = np.load('planet_e_position_0.npy')
planet_b_position = np.load('planet_b_position_0.npy')
star_position = np.load('star_position_0.npy')

#Load the results form the different simulations and add them together.
↪  Delete them afterwards.
for i in simulation_numbers:
    zwischen = np.load(f'position_{i}.npy')
    position[:,i, :] = zwischen[:,0,:]
    zwischen = np.load(f'velocity_{i}.npy')
    velocity[:,i, :] = zwischen[:,0,:]
    zwischen = np.load(f'Particle_radius_{i}.npy')
    Particle_radius[i, :] = zwischen[0,:]
    zwischen = np.load(f'Particle_temperature_{i}.npy')
    Particle_temperature[i, :] = zwischen[0,:]
    zwischen = np.load(f'Particle_beta_{i}.npy')
    Particle_beta[i, :] = zwischen[0,:]
    os.remove(f'position_{i}.npy')
    os.remove(f'velocity_{i}.npy')
    os.remove(f'Particle_radius_{i}.npy')
    os.remove(f'Particle_temperature_{i}.npy')
    os.remove(f'Particle_beta_{i}.npy')
    os.remove(f'planet_e_position_{i}.npy')
    os.remove(f'planet_b_position_{i}.npy')
    os.remove(f'star_position_{i}.npy')


direction ='all'
name_ending = 'Valdes_paramerters'

#Save the Results of all the simulations together:
np.save("Dust_position.npy", position)
np.save("Dust_velocity.npy", velocity)
np.save("Planet_e_position.npy", planet_e_position)
np.save("Planet_b_position.npy", planet_b_position)
np.save("Star_position.npy", star_position)
```

```
np.save("Dust_radius.npy", Particle_radius)
np.save("Dust_temperature.npy", Particle_temperature)
np.save("Dust_beta.npy", Particle_beta)
```

References

Andrault, D., Monteux, J., Le Bars, M., and Samuel, H. (2016). The deep earth may not be cooling down. *Earth and Planetary Science Letters*, 443:195–203.

Aschwanden, M. J. (2018). Self-organizing systems in planetary physics: Harmonic resonances of planet and moon orbits. *New Astronomy*, 58:107–123.

Becker, J. C., Vanderburg, A., Adams, F. C., Rappaport, S. A., and Schwengeler, H. M. (2015). WASP-47: A HOT JUPITER SYSTEM WITH TWO ADDITIONAL PLANETS DISCOVERED BY k2. *The Astrophysical Journal*, 812(2):L18.

Beckett, F., Rossi, E., Devenish, B., Witham, C., and Bonadonna, C. (2022). Modelling the size distribution of aggregated volcanic ash and implications for operational atmospheric dispersion modelling. *Atmospheric Chemistry and Physics*, 22(5):3409–3431.

Bolmont, E., Selsis, F., Raymond, S. N., Leconte, J., Hersant, F., Maurin, A.-S., and Pericaud, J. (2013). Tidal dissipation and eccentricity pumping: Implications for the depth of the secondary eclipse of 55 cancri e. *Astronomy &amp Astrophysics*, 556:A17.

Bourrier, Vincent and Hébrard, Guillaume (2014). Detecting the spin-orbit misalignment of the super-earth 55 cancri e. *A&A*, 569:A65.

Brogi, M., Keller, C. U., de Juan Ovelar, M., Kenworthy, M. A., de Kok, R. J., Min, M., and Snellen, I. A. G. (2012). Evidence for the disintegration of KIC 12557548 b. *Astronomy &amp Astrophysics*, 545:L5.

Butler, R. P., Marcy, G. W., Williams, E., Hauser, H., and Shirts, P. (1997). Three new "51 pegasi-type" planets*. *The Astrophysical Journal*, 474(2):L115.

Charbonneau, D., Brown, T. M., Latham, D. W., and Mayor, M. (2000). Detection of planetary transits across a sun-like star. *The Astrophysical Journal*, 529(1):L45–L48.

Currie, T. and Hansen, B. (2007). The evolution of protoplanetary disks around millisecond pulsars: The PSR 125712 system. *The Astrophysical Journal*, 666(2):1232–1244.

Deck, K. M., Agol, E., Holman, M. J., and Nesvorný , D. (2014). TTVFast: AN EFFICIENT AND ACCURATE CODE FOR TRANSIT TIMING INVERSION PROBLEMS. *The Astrophysical Journal*, 787(2):132.

Demory, B.-O., Gillon, M., de Wit, J., Madhusudhan, N., Bolmont, E., Heng, K., Kataria, T., Lewis, N., Hu, R., Krick, J., Stamenković, V., Benneke, B., Kane, S., and Queloz, D. (2016). A map of the large day–night temperature gradient of a super-earth exoplanet. *Nature*, 532(7598):207–209.

Demory, B.-O., Gillon, M., Deming, D., Valencia, D., Seager, S., Benneke, B., Lovis, C., Cubillos, P., Harrington, J., Stevenson, K. B., Mayor, M., Pepe, F., Queloz, D., Sé gransan, D., and Udry, S. (2011). Detection of a transit of the super-earth 55 cancri e with warm ispitzer/i. *Astronomy &amp Astrophysics*, 533:A114.

Demory, B.-O., Gillon, M., Madhusudhan, N., and Queloz, D. (2016). Variability in the super-Earth 55 Cnc e. , 455(2):2018–2027.

Demory, B.-O., Sulis, S., Meier Valdés, E., Delrez, L., Brandeker, A., Billot, N., Fortier, A., Hoyer, S., Sousa, S. G., Heng, K., Lendl, M., Krenn, A., Morris, B. M., Patel, J. A., Alibert, Y., Alonso, R., Anglada, G., Bárczy, T., Barrado, D., Barros, S. C. C., Baumjohann, W., Beck, M., Beck, T., Benz, W., Bonfils, X., Broeg, C., Buder, M., Cabrera, J., Charnoz, S., Collier Cameron, A., Cottard, H., Csizmadia, Sz., Davies, M. B., Deleuil, M., Demangeon, O. D. S., Ehrenreich, D., Erikson, A., Fossati, L., Fridlund, M., Gandolfi, D., Gillon, M., Güdel, M., Isaak, K. G., Kiss, L. L., Laskar, J., Lecavelier des Etangs, A., Lovis, C., Luntzer, A., Magrin, D., Marafatto, L., Maxted, P. F. L., Nascimbeni, V., Olofsson, G., Ottensamer, R., Pagano, I., Pallé, E., Peter, G., Piotto, G., Pollacco, D., Queloz, D., Ragazzoni, R., Rando, N., Ratti, F., Rauer, H., Ribas, I., Santos, N. C., Scandariato, G., Ségransan, D., Simon, A. E., Smith, A. M. S., Steller, M., Szabó, Gy. M., Thomas, N., Udry, S., Van Grootel, V., and Walton, N. A. (2023). 55 cancri e´s occultation captured with cheops. *A&A*, 669:A64.

Ehrenreich, D., Bourrier, V., Bonfils, X., des Etangs, A. L., Hébrard, G., Sing, D. K., Wheatley, P. J., Vidal-Madjar, A., Delfosse, X., Udry, S., Forveille, T., and Moutou, C. (2012). Hint of a transiting extended atmosphere on 55 cancri b. *Astronomy &amp Astrophysics*, 547:A18.

Eyre, D. and Miller, H. (1990). Treatment of continuum effects via a generalized gauss quadrature. *Physics Letters B*, 235(3):229–233.

Fabian, A. C. and Podsiadlowski, P. (2003). Binary precursor for planet? *Nature*, 353(6347):801.

Fischer, D. A., Marcy, G. W., Butler, R. P., Vogt, S. S., Laughlin, G., Henry, G. W., Abouav, D., Peek, K. M. G., Wright, J. T., Johnson, J. A., McCarthy, C., and Isaacson, H. (2008). Five planets orbiting 55 cancri. *The Astrophysical Journal*, 675(1):790–801.

Folsom, C. P., Fionnagáin, D. Ó ., Fossati, L., Vidotto, A. A., Moutou, C., Petit, P., Dragomir, D., and Donati, J.-F. (2020). Circumstellar environment of 55 cancri. *Astronomy &amp Astrophysics*, 633:A48.

Gauß, C. F. (1815). Methodus nova integralium valores per approximationem inveniendi. *Comm. Soc. Sci. Göttingen Math*, 3:29–76.

Gelman, S. E., Elkins-Tanton, L. T., and Seager, S. (2011). Effects of stellar flux on tidally locked terrestrial planets: Degree-1 mantle convection and local magma ponds. *The Astrophysical Journal*, 735(2):72.

Grimm, Simon L., Demory, Brice-Olivier, Gillon, Michaël, Dorn, Caroline, Agol, Eric, Burdanov, Artem, Delrez, Laetitia, Sestovic, Marko, Triaud, Amaury H. M. J., Turbet, Martin, Bolmont, Émeline, Caldas, Anthony, de Wit, Julien, Jehin, Emmanuël, Leconte, Jérémy, Raymond, Sean N., Van Grootel, Valérie, Burgasser, Adam J., Carey, Sean, Fabrycky, Daniel, Heng, Kevin, Hernandez, David M., Ingalls, James G., Lederer, Susan, Selsis, Franck, and Queloz, Didier (2018). The nature of the trappist-1 exoplanets. *A&A*, 613:A68.

Hammond, M. and Pierrehumbert, R. T. (2017). Linking the climate and thermal phase curve of 55 cancri e. *The Astrophysical Journal*, 849(2):152.

Hans-Peter Gail, E. S. (2013). *Physics and Chemistry of Circumstellar Dust Shells*. Cambridge University Press, Cambridge.

Hansen, B. M. S. (2022). Consequences of dynamically unstable moons in extrasolar systems. *Monthly Notices of the Royal Astronomical Society*, 520(1):761–772.

Hansen, B. M. S. and Zink, J. (2015). On the potentially dramatic history of the super-earth 55 cancri e. *Monthly Notices of the Royal Astronomical Society*, 450(4):4505–4520.

Hellier, C., Anderson, D. R., Cameron, A. C., Doyle, A. P., Fumel, A., Gillon, M., Jehin, E., Lendl, M., Maxted, P. F. L., Pepe, F., Pollacco, D., Queloz, D., Sé gransan, D., Smalley, B., Smith, A. M. S., Southworth, J., Triaud, A. H. M. J., Udry, S., and West, R. G. (2012). Seven transiting hot jupiters from WASP-south, euler and TRAPPIST: WASP-47b, WASP-55b, WASP-61b, WASP-62b, WASP-63b, WASP-66b and WASP-67b. *Monthly Notices of the Royal Astronomical Society*, 426(1):739–750.

Hildebrand, F. B. (1956). *Introduction to Numerical Analysis*. McGraw-Hil, New York.

Holman, M. J. and Murray, N. W. (2005). The use of transit timing to detect terrestrial-mass extrasolar planets. *Science*, 307(5713):1288–1291.

Jackson, B., Barnes, R., and Greenberg, R. (2008). Tidal heating of terrestrial extrasolar planets and implications for their habitability. *Monthly Notices of the Royal Astronomical Society*, 391(1):237–245.

Jacobi, C. G. J. (1826). Ueber gauß' neue methode, die werthe der integrale näherungsweise zu finden. *Journal für Reine und Angewandte Mathematik*, 1:301–308.

Jayawardhana, R., Holland, W. S., Greaves, J. S., Dent, W. R. F., Marcy, G. W., Hartmann, L. W., and Fazio, G. G. (2000). Dust in the 55 cancri planetary system. *The Astrophysical Journal*, 536(1):425–428.

Jiayin Dong, Songhu Wang, M. R. G. Z. C. X. H. R. I. D. G. K. S. S. H. S. K. S. M. (2023). Toi-1859b: A 64 day warm jupiter on an eccentric and misaligned orbit. *The Astrophysical Journal Letters*, 951.

Josette Wright, Malena Rice, X.-Y. W. K. H. and Wang, S. (2006). Soles. vii. the spin–orbit alignment of wasp-106 b, a warm jupiter along the kraft break. *The Astronomical Journal*, 166.

Josette Wright, Malena Rice, X.-Y. W. K. H. and Wang, S. (2023). Soles. vii. the spin–orbit alignment of wasp-106 b, a warm jupiter along the kraft break. *The Astronomical Journal*, 166.

Keles, E., Mallonn, M., Kitzmann, D., Poppenhaeger, K., Hoeijmakers, H. J., Ilyin, I., Alexoudi, X., Carroll, T. A., Alvarado-Gomez, J., Ketzer, L., Bonomo, A. S., Borsa, F., Gaudi, B. S., Henning, T., Malavolta, L., Molaverdikhani, K., Nascimbeni, V., Patience, J., Pino, L., Scandariato, G., Schlawin, E., Shkolnik, E., Sicilia, D., Sozzetti, A., Foster, M. G., Veillet, C., Wang, J., Yan, F., and Strassmeier, K. G. (2022). The PEPSI exoplanet transit survey (PETS) i: investigating the presence of a silicate atmosphere on the super-earth 55 cnc e. *Monthly Notices of the Royal Astronomical Society*, 513(1):1544–1556.

Kimura, H., Okamoto, H., and Mukai, T. (2002). Radiation pressure and the poynting–robertson effect for fluffy dust particles. *Icarus*, 157(2):349–361.

Kirchschlager, F. and Wolf, S. (2013). Porous dust grains in debris disks. *Astronomy &amp Astrophysics*, 552:A54.

Kitzmann, D. and Heng, K. (2017). Optical properties of potential condensates in exoplanetary atmospheres.

Kobayashi, H., Kimura, H., ichiro Watanabe, S., Yamamoto, T., and Müller, S. (2011). Sublimation temperature of circumstellar dust particles and its importance for dust ring formation. *Earth, Planets and Space*, 63(10):1067–1075.

Konacki, M. and Wolszczan, A. (2003). Masses and orbital inclinations of planets in the PSR b125712 system. *The Astrophysical Journal*, 591(2):L147–L150.

Krishnan, G., Achyuthan, H., and Siva, V. (2017). Comparative petrophysical and geochemical characteristics of thermal and volcanic ash from southeastern india. *Journal of the Geological Society of India*, 90:20–24.

Kyle Hixenbaugh, Xian-Yu Wang, M. R. S. W. (2023). The spin–orbit misalignment of toi-1842b: The first measurement of the rossiter–mclaughlin effect for a warm sub-saturn around a massive star. *The Astrophysical Journal Letters*, 949.

Li, B., Zhang, L., Su, T., Han, X. L., Misra, P., and Long, L. (2023). Statistical and radio analysis of exoplanets and their host stars. *Universe*, 9(11).

López-Morales, M., Triaud, A. H. M. J., Rodler, F., Dumusque, X., Buchhave, L. A., Harutyunyan, A., Hoyer, S., Alonso, R., Gillon, M., Kaib, N. A., Latham, D. W., Lovis, C., Pepe, F., Queloz, D., Raymond, S. N., Ségransan, D., Waldmann, I. P., and Udry, S. (2014). ROSSITER-MCLAUGHLIN OBSERVATIONS OF 55 cnc e. *The Astrophysical Journal*, 792(2):L31.

Löhne, T., Krivov, A. V., Kirchschlager, F., Sende, J. A., and Wolf, S. (2017). Collisions and drag in debris discs with eccentric parent belts. *AA*, 605:A7.

Marcy, G. W., Butler, R. P., Fischer, D. A., Laughlin, G., Vogt, S. S., Henry, G. W., and Pourbaix, D. (2002). A planet at 5 AU around 55 cancri. *The Astrophysical Journal*, 581(2):1375–1388.

Mayor, M. and Queloz, D. (1995). A jupiter-mass companion to a solar-type star. *Nature*, 378:355–359.

McArthur, B. E., Endl, M., Cochran, W. D., Benedict, G. F., Fischer, D. A., Marcy, G. W., Butler, R. P., Naef, D., Mayor, M., Queloz, D., Udry, S., and Harrison, T. E. (2004). Detection of a neptune-mass planet in the sup1/sup cancri system using the hobby-eberly telescope. *The Astrophysical Journal*, 614(1):L81–L84.

Milton Abramowitz, I. A. S. (1965). *Handbook of Mathematical Functions with Formulas, Graphs, and Mathematical Tables*. Dover, New York.

Nelson, B. E., Ford, E. B., Wright, J. T., Fischer, D. A., von Braun, K., Howard, A. W., Payne, M. J., and Dindar, S. (2014). The 55 cancri planetary system: fully self-consistent n-body constraints and a dynamical analysis. *Monthly Notices of the Royal Astronomical Society*, 441(1):442–451.

Neveu-VanMalle, M., Queloz, D., Anderson, D. R., Brown, D. J. A., Cameron, A. C., Delrez, L., Dí az, R. F., Gillon, M., Hellier, C., Jehin, E., Lister, T., Pepe, F., Rojo, P., Ségransan, D., Triaud, A. H. M. J., Turner, O. D., and Udry, S. (2016). Hot jupiters with relatives: discovery of additional planets in orbit around WASP-41 and WASP-47. *Astronomy &amp Astrophysics*, 586:A93.

Niţu, I. C., Keith, M. J., Stappers, B. W., Lyne, A. G., and Mickaliger, M. B. (2022). A search for planetary companions around 800 pulsars from the jodrell bank pulsar timing programme. *Monthly Notices of the Royal Astronomical Society*, 512(2):2446–2459.

Radau, R. (1880). Etude sur les formules d'approximation qui servent à calculer la valeur numérique d'une intégrale définie. *J. Math. Pures et Appl.*, 6:283–336.

Raghavan, D., Henry, T. J., Mason, B. D., Subasavage, J. P., Jao, W.-C., Beaulieu, T. D., and Hambly, N. C. (2006). Two suns in the sky: Stellar multiplicity in exoplanet systems. *The Astrophysical Journal*, 646(1):523–542.

Rappaport, S., Levine, A., Chiang, E., Mellah, I. E., Jenkins, J., Kalomeni, B., Kite, E. S., Kotson, M., Nelson, L., Rousseau-Nepton, L., and Tran, K. (2012). POSSIBLE DISINTEGRATING SHORT-PERIOD SUPER-MERCURY ORBITING KIC 12557548. *The Astrophysical Journal*, 752(1):1.

Rein, H. and Liu, S.-F. (2012). REBOUND: an open-source multi-purposein/i-body code for collisional dynamics. *Astronomy &amp Astrophysics*, 537:A128.

Rein, H. and Spiegel, D. S. (2014). ias15: a fast, adaptive, high-order integrator for gravitational dynamics, accurate to machine precision over a billion orbits. *Monthly Notices of the Royal Astronomical Society*, 446(2):1424–1437.

Rein, H. and Winkler, L. (2021). Calculating transit timing variations (ttv) with rebound.

Schweitzer, A., Passegger, V. M., Cifuentes, C., Bé jar, V. J. S., Cortés-Contreras, M., Caballero, J. A., del Burgo, C., Czesla, S., Kürster, M., Montes, D., Osorio, M. R. Z., Ribas, I., Reiners, A., Quirrenbach, A., Amado, P. J., Aceituno, J., Anglada-Escudé, G., Bauer, F. F., Dreizler, S., Jeffers, S. V., Guenther, E. W., Henning, T., Kaminski, A., Lafarga, M., Marfil, E., Morales, J. C., Schmitt, J. H. M. M., Seifert, W., Solano, E., Tabernero, H. M., and Zechmeister, M. (2019). The CARMENES search for exoplanets around m dwarfs. *Astronomy &amp Astrophysics*, 625:A68.

Smadar Naoz, Will M. Farr, F. A. R. (2012). On the formation of hot jupiters in stellar binaries. *The Astrophysical Journal Letters*, 754.

Sucerquia, M., Alvarado-Montes, J. A., Bayo, A., Cuadra, J., Cuello, N., Giuppone, C. A., Montesinos, M., Olofsson, J., Schwab, C., Spitler, L., and Zuluaga, J. I. (2021). icronomoons/i: origin, dynamics, and light-curve features of ringed exomoons. *Monthly Notices of the Royal Astronomical Society*, 512(1):1032–1044.

Sulis, S., Dragomir, D., Lendl, M., Bourrier, V., Demory, B. O., Fossati, L., Cubillos, P. E., Guenther, D. B., Kane, S. R., Kuschnig, R., Matthews, J. M., Moffat, A. F. J., Rowe, J. F., Sasselov, D., Weiss, W. W., and Winn, J. N. (2019). Multi-season optical modulation phased with the orbit of the super-earth 55 cancri e. *Astronomy &amp Astrophysics*, 631:A129.

Taddeucci, J., Alatorre-Ibargüengoitia, M. A., Cruz-Vázquez, O., Del Bello, E., Scarlato, P., and Ricci, T. (2017). In-flight dynamics of volcanic ballistic projectiles. *Reviews of Geophysics*, 55(3):675–718.

Tamayo, D., Rein, H., Shi, P., and Hernandez, D. M. (2019). REBOUNDx: a library for adding conservative and dissipative forces to otherwise symplectic n-body integrations. *Monthly Notices of the Royal Astronomical Society*, 491(2):2885–2901.

Tokadjian, A. and Piro, A. L. (2020). Impact of tides on the potential for exoplanets to host exomoons. *The Astronomical Journal*, 160(4):194.

Tokadjian, A. and Piro, A. L. (2023). Tidal heating of exomoons in resonance and implications for detection. *The Astronomical Journal*, 165(4):173.

Trilling, D. E. and Brown, R. H. (1998). A circumstellar dust disk around a star with a known planetary companion. , 395(6704):775–777.

Tsiaras, A., Rocchetto, M., Waldmann, I. P., Venot, O., Varley, R., Morello, G., Damiano, M., Tinetti, G., Barton, E. J., Yurchenko, S. N., and Tennyson, J. (2016). DETECTION OF AN ATMOSPHERE AROUND THE SUPER-EARTH 55 CANCRI e. *The Astrophysical Journal*, 820(2):99.

Valdés, E. A. M., Morris, B. M., Demory, B. O., Brandeker, A., Kitzmann, D., Benz, W., Deline, A., Florén, H. G., Sousa, S. G., Bourrier, V., Singh, V., Heng, K., Strugarek, A., Bower, D. J., Jäggi, N., Carone, L., Lendl, M., Jones, K., Oza, A. V., Demangeon, O. D. S., Alibert, Y., Alonso, R., Anglada, G., Asquier, J., Bárczy, T., Navascues, D. B., Barros, S. C. C., Baumjohann, W., Beck, M., Beck, T., Billot, N., Bonfils, X., Borsato, L., Broeg, C., Cabrera, J., Charnoz, S., Cameron, A. C., Csizmadia, S., Cubillos, P. E., Davies, M. B., Deleuil, M., Delrez, L., Ehrenreich, D., Erikson, A., Fortier, A., Fossati, L., Fridlund, M., Gandolfi, D., Gillon, M., Güdel, M., Günther, M. N., Hoyer, S., Isaak, K. G., Kiss, L. L., Laskar, J., des Etangs, A. L., Lovis, C., Magrin, D., Maxted, P. F. L., Mordasini, C., Nascimbeni, V., Olofsson, G., Ottensamer, R., Pagano, I., Pallé, E., Peter, G., Piotto, G., Pollacco, D., Queloz, D., Ragazzoni, R., Rando, N., Rauer, H., Ribas, I., Santos, N. C., Sarajlic, M., Scandariato, G., Ségransan, D., Sicilia, D., Simon, A. E., Smith, A. M. S., Steller, M., Szabó, G. M., Thomas, N., Udry, S., Ulmer, B., Grootel, V. V., Venturini, J., Walton, N. A., Wilson, T. G., and Wolter, D. (2023). Investigating the visible phase-curve variability of 55 cnc e.

van Lieshout, R., Min, M., and Dominik, C. (2014). Dusty tails of evaporating exoplanets. *Astronomy &amp Astrophysics*, 572:A76.

Vanderburg, A., Becker, J. C., Buchhave, L. A., Mortier, A., Lopez, E., Malavolta, L., Haywood, R. D., Latham, D. W., Charbonneau, D., Ló pez-Morales, M., Adams, F. C., Bonomo, A. S., Bouchy, F., Cameron, A. C., Cosentino, R., Fabrizio, L. D., Dumusque, X., Fiorenzano, A., Harutyunyan, A., Johnson, J. A., Lorenzi, V., Lovis, C., Mayor, M., Micela, G., Molinari, E., Pedani, M., Pepe, F., Piotto, G., Phillips, D., Rice, K., Sasselov, D., Ségransan, D., Sozzetti, A., Udry, S., and Watson, C. (2017). Precise masses in the WASP-47 system. *The Astronomical Journal*, 154(6):237.

Weiss, L. M., Deck, K. M., Sinukoff, E., Petigura, E. A., Agol, E., Lee, E. J., Becker, J. C., Howard, A. W., Isaacson, H., Crossfield, I. J. M., Fulton, B. J., Hirsch, L., and Benneke, B. (2017). New insights on planet formation in WASP-47 from a simultaneous analysis of radial velocities and transit timing variations. *The Astronomical Journal*, 153(6):265.

Winn, J. N., Matthews, J. M., Dawson, R. I., Fabrycky, D., Holman, M. J., Kallinger, T., Kuschnig, R., Sasselov, D., Dragomir, D., Guenther, D. B., Moffat, A. F. J., Rowe, J. F., Rucinski, S., and Weiss, W. W. (2011). A SUPER-EARTH TRANSITING a NAKED-EYE STAR. *The Astrophysical Journal*, 737(1):L18.

Wolszczan, A. (1994). Confirmation of earth-mass planets orbiting the millisecond pulsar psr b1257 + 12. *Science*, 264(5158):538–542.

Wolszczan, A. and Frail, D. A. (1992). A planetary system around the millisecond pulsar psr1257 + 12. *Nature*, 355:145–147.

Zandt, J. V., Petigura, E. A., MacDougall, M., Gilbert, G. J., Lubin, J., Barclay, T., Batalha, N. M., Crossfield, I. J. M., Dressing, C., Fulton, B., Howard, A. W., Huber, D., Isaacson, H., Kane, S. R., Robertson, P., Roy, A., Weiss, L. M., Behmard, A., Beard, C., Chontos, A., Dai, F., Dalba, P. A., Fetherolf, T., Giacalone, S., Henze, C. E., Hill, M. L., Hirsch, L. A., Holcomb, R., Howell, S. B., Jenkins, J. M., Latham, D. W., Mayo, A., Mireles, I., Moč nik, T., Murphy, J. M. A., Pidhorodetska, D., Polanski, A. S., Ricker, G. R., Rosenthal, L. J., Rubenzahl, R. A., Seager, S., Scarsdale, N., Turtelboom, E. V., Vanderspek, R., and Winn, J. N. (2023). TESS-keck survey. XIV. two giant exoplanets from the distant giants survey. *The Astronomical Journal*, 165(2):60.

Zhang, M., Knutson, H. A., Wang, L., Dai, F., Oklopcic, A., and Hu, R. (2021). No escaping helium from 55 cnc e∗.$TheAstronomicalJournal$, 161(4) : 181.

Zhao, L. L., Kunovac, V., Brewer, J. M., Llama, J., Millholland, S. C., Hedges, C., Szymkowiak, A. E., Roettenbacher, R. M., Cabot, S. H. C., Weiss, S. A., and Fischer, D. A. (2022). Measured spin–orbit alignment of ultra-short-period super-earth 55 cancri e. *Nature Astronomy*.